Highly efficient nitrogen-doped reduced graphene oxide-$Sr_{0.7}Sm_{0.3}Fe_{0.4}Co_{0.6}O_{2.65}$ nanocomposites utilized as a counter electrode in dye-sensitized solar cells

Samantha Ndlovu, Edigar Muchuweni, Moses A. Ollengo, Vincent O. Nyamori

PII: S2352-4928(23)02372-3

DOI: https://doi.org/10.1016/j.mtcomm.2023.107681

Reference: MTCOMM107681

To appear in: *Materials Today Communications*

Received date: 7 December 2022
Revised date: 20 November 2023
Accepted date: 23 November 2023

Please cite this article as: Samantha Ndlovu, Edigar Muchuweni, Moses A. Ollengo and Vincent O. Nyamori, Highly efficient nitrogen-doped reduced graphene oxide-$Sr_{0.7}Sm_{0.3}Fe_{0.4}Co_{0.6}O_{2.65}$ nanocomposites utilized as a counter electrode in dye-sensitized solar cells, *Materials Today Communications,* (2023) doi:https://doi.org/10.1016/j.mtcomm.2023.107681

Highly efficient nitrogen-doped reduced graphene oxide-$Sr_{0.7}Sm_{0.3}Fe_{0.4}Co_{0.6}O_{2.65}$ nanocomposites utilized as a counter electrode in dye-sensitized solar cells

Samantha Ndlovu, Edigar Muchuweni[†], Moses A. Ollengo and Vincent O. Nyamori*

School of Chemistry and Physics, University of KwaZulu-Natal, Westville Campus, Private Bag X54001, Durban 4000, South Africa

[†]On leave from Bindura University of Science Education, Department of Engineering and Physics, Private Bag 1020, Bindura, Zimbabwe

*Corresponding author: nyamori@ukzn.ac.za; Tel.: +27-31-2608256; Fax: +27-312603091

Email addresses of co-authors: samanthandlovu36@gmail.com, emuchuweni@buse.ac.zw

Abstract

Dye-sensitized solar cells (DSSCs) are known for their aesthetic properties, not limited to colour tuneability and transparency, but are also promising renewable energy technology that can efficiently harvest sunlight to generate electricity without releasing toxic gases. DSSCs are one of the potential candidates for fabricating colourful and see-through solar cells for energy-harvesting aesthetic windows. However, a trade-off between transparency and power conversion efficiency (PCE) has to be tackled amicably to realize solar cells with good PCE and transparency. Judicious selection of dyes to bypass light absorption in the high eye-sensitivity region (500 – 600 nm) is one of the plausible solutions. Most importantly, developing novel counter electrode materials using facile preparation techniques, low-cost materials, and environmentally friendly conditions helps overcome the limitations of commonly used but expensive and corroding metals, thereby improving the PCE of DSSCs. Herein, we report the synthesis of a novel hybrid nitrogen-doped reduced graphene oxide-$Sr_{0.7}Sm_{0.3}Fe_{0.4}Co_{0.6}O_{2.65}$ (N-RGO-SSFC) nanocomposite using the thermal treatment method. The N-RGO-SSFC nanocomposites were characterized using microscopic and spectroscopic techniques and applied as counter electrodes in DSSCs. Scanning electron microscopy images revealed the presence of N-RGO sheets decorated by SSFC nanoparticles. The introduction of SSFC nanoparticles onto N-RGO sheets led to the formation of nanocomposites with a tetragonal structure, a surface area of 178.0 $m^2\ g^{-1}$, an electrical conductivity of 13.02 S cm^{-1}, and a charge transfer resistance of 10.6 Ω. The N-RGO-SSFC

nanocomposite counter electrodes resulted in DSSCs with an enhanced PCE of 6.64% due to the formation of excellent electron transfer pathways. This outperformed DSSCs based on the Pt reference electrode with a PCE of 5.52%. Hence, N-RGO-SSFC nanocomposites can be applied as a potential counter-electrode material in DSSCs.

Graphical abstract

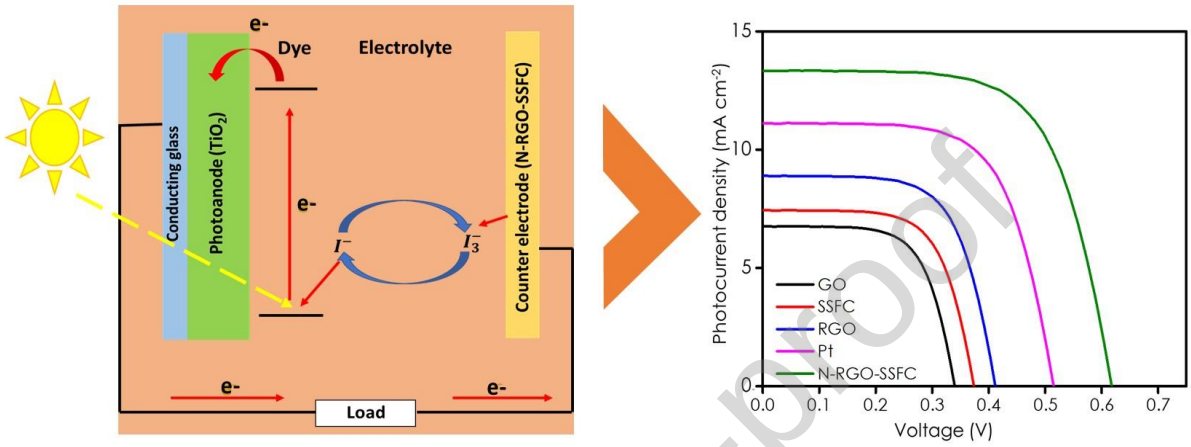

Keywords: Nanocomposites; Reduced graphene oxide; Perovskite oxides; Photovoltaics; Dye-sensitized solar cells

1. Introduction

The current lower solar-to-electrical energy conversion efficiency and photovoltaic performance stability have prevented dye-sensitized solar cells (DSSCs) from successfully competing with the existing commercial photovoltaic (PV) technologies for bulk electricity generation outdoors. What is not in doubt is the capability of DSSCs to be manufactured as thin and lightweight flexible solar modules, projecting an ideal solution for portable electronics. Their other main advantage is the ability to have a relatively good power conversion efficiency (PCE) under dim light, outperforming traditional technologies in typical indoor and outdoor conditions [1]. This is a suitable plugin for ambient energy harvesting for the wireless sensors used in the Internet of Things (IoT) devices [2]. However, low-power IoT sensing applications need self-powered sensors. Hence, power management of such self-powered sensors, in terms of the energy consumed, is critical to efficiency [3]. Other fronts have been investigated to overcome harvesting challenges. Tunability is considered one of the main advantages of DSSCs over conventional Si-based solar cells. The thickness of the active layer has been varied to enhance cell transparency. Whereas this has

a cost implication on cell efficiency, DSSCs, with tailored transparency, could be utilized in photovoltaic window applications, where Si cells are barely suitable [4].

In addition, DSSCs are widely studied due to their low cost, facile preparation processes, environmental friendliness, and a promising PCE that can be improved when compared to other solar cells [2]. DSSCs consist of three main parts, *viz.*, the mesoporous photoanode film, which is sensitized using dye, an electrolyte with the iodide/triiodide (I^-/I_3^-) redox couple and a counter electrode [5]. The mesoporous titanium dioxide (TiO_2) has been mostly used as the photoanode film to adsorb dye molecules [6]. The dye is the most crucial component for DSSC device operation, which is covalently bonded to the mesoporous oxide layer surface. The dye functions as a molecular electron pump that absorbs visible light to generate electrons before transporting them into the semiconductor [7]. Ruthenium-based dyes, such as N3 [8], N719 [9], and Z907 [8], have resulted in devices with promising PCEs of up to 12.1% [10]. These harvesters have shown outstanding photovoltaic performances due to their broad absorption spectra. Although ruthenium dyes showed advantageous qualities of high efficiency, their usage can be limited by availability as well as high cost. To circumvent these limitations, researchers have shifted focus on developing metal-free organic dyes, such as D-pi-A structured organic dyes [11-14], due to their relatively lower cost, excellent electrochemical properties, and good optical properties with an efficiency of more than 14.2% [15,16]. Co-sensitization of metal-free organic dyes with porphyrin has enhanced the PCE of DSSCs to 12.3%, due to the harvesting of light across the visible spectrum, which allows for the generation of a large photocurrent [17]. On the other side, an electrolyte such as iodine is accountable for the redox reaction to determine electrons that will reduce and regenerate the oxidized dye [18,19].

The counter electrode plays a vital role in collecting electrons from the external circuit and acts as an electrocatalyst to activate the reduction of I^-/I_3^- ions or any other oxidized redox species [20,21]. Typically, platinum (Pt) is the most preferred DSSC counter electrode due to its excellent catalytic activity [22] and excellent electrocatalytic activity [23,24], which results in high PCEs. However, the usage of Pt has been set back by several issues, such as its high cost and scarcity, which limit the large-scale production of DSSCs [25]. To mitigate these issues, it would be in the best interest to use alternative materials that have excellent catalytic activity for reducing I_3^- ions [26], at the same time, have the benefit of high electrical

conductivity, being environmentally friendly, and still having low cost relative to metals such as Pt while producing DSSCs with superior performance.

In the last decade, carbon-based materials [27-31], such as carbon nanotubes (CNTs) [32], Te-doped mesoporous carbon black (CB) [33,34], nitrogen-enriched nanocarbons [35], and graphene [36-38], have emerged as potential substitutes for Pt counter electrodes in DSSCs [39]. Among these, graphene has been most preferred due to its single-layer honeycomb lattice with sp^2 hybridized carbon atoms, which can possess high specific surface area [40], excellent chemical stability [41], superior mechanical flexibility [42], and unique catalytic activity [43]. These various properties allow graphene to be easily used as the catalytic film for the DSSC counter electrode [26]. Chu et al. [44] fabricated DSSCs with reduced graphene oxide (RGO) as the counter electrode and obtained a PCE of 2.07%, which was comparable to 3.64% for the Pt counter electrode-based device. However, using graphene as a counter electrode in DSSCs can be limited by its wettability and inert nature, which affect charge transfer at the graphene/electrolyte interface [45,46]. On the other side, graphene is hydrophobic and can easily be restacked, which can restrict the interconnectivity of the solvent on the material, thereby negatively affecting device performance [47]. It is essential to create active catalytic sites on graphene to reduce I_3^- effectively and also to tune the bandgap by altering the surface chemistry of graphene [48]. Introducing heteroatoms, such as boron, phosphorus [39] and nitrogen [21,49], into graphene can cause electron modulation [50], improving the electronic structure and catalytic activity [51,52]. These various heteroatoms have similar sizes and atomic radii, which affect the electron chemistry through the graphene framework to confer electrical properties with either p- or n-type conductivity [49,53,54].

On the other hand, using heteroatom-doped graphene as support for perovskites can produce synergistic coupling between the materials [55,56]. Generally, perovskite oxides are formed from mixed oxides with the formula ABO_3, where the A- and B-sites can be partially substituted with larger alkali/rare earth metal ions and smaller transition metal ions, respectively [57]. On ABO_3, the A-site cations are positioned at the central body of the cubic structure, and the B-site cations are placed at the cubic corner positions, whereas the oxide anions are situated at the face-centred positions [57]. Perovskites (ABO_3) have been used in many applications due to their excellent properties, such as high electrochemical stability [58], high electrical conductivity [59], and superior catalytic activity [60,61]. Researchers

have tried different methods, such as hydrothermal [62,63], co-precipitation [64], sol-gel [65], combustion [66], and ultra-sonication [67], to prepare perovskite oxide nanocomposites with exceptional properties [59]. For example, Xiong et al. [68] synthesized $La_{0.65}Sr_{0.35}MnO_3$-reduced graphene oxide (LCMO-RGO) nanocomposites using a solution combustion method and used the LCMO-RGO nanocomposite as a counter electrode in DSSCs which exhibited a high PCE of 6.57%. The strong synergistic effect between LCMO and RGO improved the catalytic activity during I_3^- reduction. Yang et al. [69] prepared LCMO nitrogen-doped RGO (LCMO-N-RGO) using the sol-gel method and employed the nanocomposite as a counter electrode in DSSCs which displayed an optimum PCE of ~7.89%. This was attributed to the high electrocatalytic activity and electrical conductivity, originating from high surface area and excellent electrical properties obtained after the addition of LCMO onto N-RGO. Thus, doped graphene-based materials as a support for perovskite oxide can function well as a counter electrode and as a replacement for Pt.

This study is the first report on the synthesis of N-RGO-$Sr_{0.7}Sm_{0.3}Fe_{0.4}Co_{0.6}O_{2.65}$ (SSFC) nanocomposites using the thermal treatment method and their application as counter electrodes in DSSCs. A comparison with DSSCs based on pristine GO, RGO, SSFC, RGO-SSFC, and Pt counter electrodes is also included to justify the preparation of N-RGO-SSFC nanocomposites. The introduction of SSFC and doping of RGO with N to form N-RGO-SSFC resulted in a strong synergistic interaction, which enhanced the nanocomposite physicochemical properties, such as surface area, optical properties, electrical properties, and electrochemical properties. DSSCs with N-RGO-SSFC counter electrodes exhibited the best PCE of 6.64%, which outperformed the devices based on pristine SSFC, GO, RGO, RGO-SSFC, and Pt (reference).

2. Experimental sections

2.1. Materials and instrumentation

Graphite powder (99.99%, trace metal basis), ammonium nitrate (97%), sodium nitrate (97%), strontium(II) acetylacetonate (97%), iron(III) acetylacetonate (97%), samarium(III) acetylacetonate hydrate (99.99%) and cobalt(III) acetylacetonate hydrate (97%), potassium permanganate (99.32%), 1-methyl-propylimidazolium iodide (98%), guanidinium thiocyanate (99%), lithium iodide (99.9%), poly(vinyl acetate) (99.9%), 4-tert-butylpyridine (96%), Eosin B (97%), and indium tin oxide (ITO) (15 Ω sq^{-1}, 30 × 45 × 0.7 mm) were all

purchased from Sigma-Aldrich (Johannesburg, South Africa). Sulfuric acid (98%) and acetonitrile (99.9%) were purchased from LabChem, the lab supplies (Gauteng, South Africa). Hydrogen peroxide (100%) and potassium permanganate (99.32%) were purchased from Promark Chemicals (Johannesburg, South Africa). A 10% ultra-high hydrogen in argon (v/v) was obtained from Afrox (Johannesburg, South Africa). The materials were weighed on the Ohaus PA214 analytical balance. All the chemicals were of an analytical grade and used without further purification.

2.2. Preparation of GO

A modified Hummers method was used to prepare GO [70,71]. Briefly, graphite powder (2 g) was added to a prepared mixture of concentrated sulfuric acid (58 ml) and sodium nitrate (2 g) in a 500 ml flask under an ice bath condition (0 °C) while stirring for 30 min. In small doses, potassium permanganate (8 g) was added slowly to the reaction mixture to avoid excessive heat. This was further stirred for 3 h. Then, hydrogen peroxide (3%) was added to the reaction under stirring for 30 min to pronounce an exothermal effect (98 °C). Lastly, the mixture was continuously washed with double distilled water to remove the excess acid and obtain a pH of 7. The product obtained was dried in an oven overnight at 80 °C and subsequently characterized.

2.3. Preparation of SSFC

Firstly, a well-mixed metal acetylacetonate (i.e., strontium(II), iron(III), samarium(III) and cobalt(III)) powder (3 g) was added into a stainless jar (250 ml), with stainless-steel balls at a ball-to-mass ratio of 13:1. High energy Retsch PM 400 MA type plenary was used to ball-mill the metal powders for 10 h at 300 rpm, using 13 balls under air conditions. The product metal powder was added into a ceramic quartz boat and heated using the Sentro Tech furnace at 600 °C for 10 h to form the SSFC perovskites.

2.4. Preparation of N-RGO-SSFC nanocomposites

The N-RGO-SSFC nanocomposite was synthesized using the thermal treatment method. This was done by adding GO (50 mg), ammonium nitrate (30 mg) as nitrogen dopant source, and SSFC (20 mg) to deionized water (15 ml), followed by sonicating for 1 h at 25 °C to make a colloidal suspension. Afterwards, the mixture was dried at 50 °C overnight to remove excess water. The solid mixture was simultaneously reduced and heat-treated using a ceramic quartz boat at 600 °C for 5 h. This was done under 10% hydrogen in argon (v/v) using the Sentro

Tech furnace at a flow rate of 100 ml min^{-1}. RGO-SSFC (100 mg) was prepared using a similar method and parameters as N-RGO-SSFC, except that no nitrogen dopant source was introduced. In brief, RGO (100 mg) was placed on the ceramic quartz boat and reduced using 10% hydrogen in argon (v/v) using similar parameters. The prepared materials were further characterized using various instrumentation.

2.5. Preparation of the photoanode, counter electrode, and gel state electrolyte

For photoanode preparation, TiO_2 (100 mg) was added to absolute ethanol (0.2 ml) and sonicated for 10 min. For counter electrode preparation, SSFC (100 mg) was added to absolute ethanol (0.2 ml), and the mixture was sonicated for 10 min. The TiO2 and SSFC mixture was deposited onto an ITO and cathode glass substrates using the doctor blade method. The prepared photoanodes and counter electrodes were annealed at 300 °C for 10 min using a hot plate. The counter electrodes were also prepared with GO, RGO, RGO-SSFC, and N-RGO-SSFC using the same preparation method for comparison purposes. The liquid electrolyte was prepared by the addition of iodine (0.0783 g), lithium iodide (0.0837 g), 4-tert-butylpyridine (0.4225 g), 1-methyl-3-propylimidazolium iodide (0.9453 g), and guanidium thiocyanate (0.0739 g) to a volumetric flask and filled with acetonitrile to the 25 ml mark. The liquid electrolyte (0.3121 g) was mixed with poly(vinyl acetate) (0.1506 g) and further mixed using a glass rod to form a gel-state electrolyte. This was then stored in a fridge until required for analysis.

2.6. Assembly of DSSCs

The prepared TiO_2 semiconductor layer on an ITO glass substrate was used as a photoanode, which was further soaked by adding Eosin B dye (0.3 mM) using a micropipette. This was followed by applying the gel-state electrolyte as the redox material. The counter electrode prepared with Pt was used as a reference. Other counter electrodes were separately prepared using SSFC, GO, RGO, RGO-SSFC, and N-RGO-SSFC. The device was assembled as shown in Fig. 1.

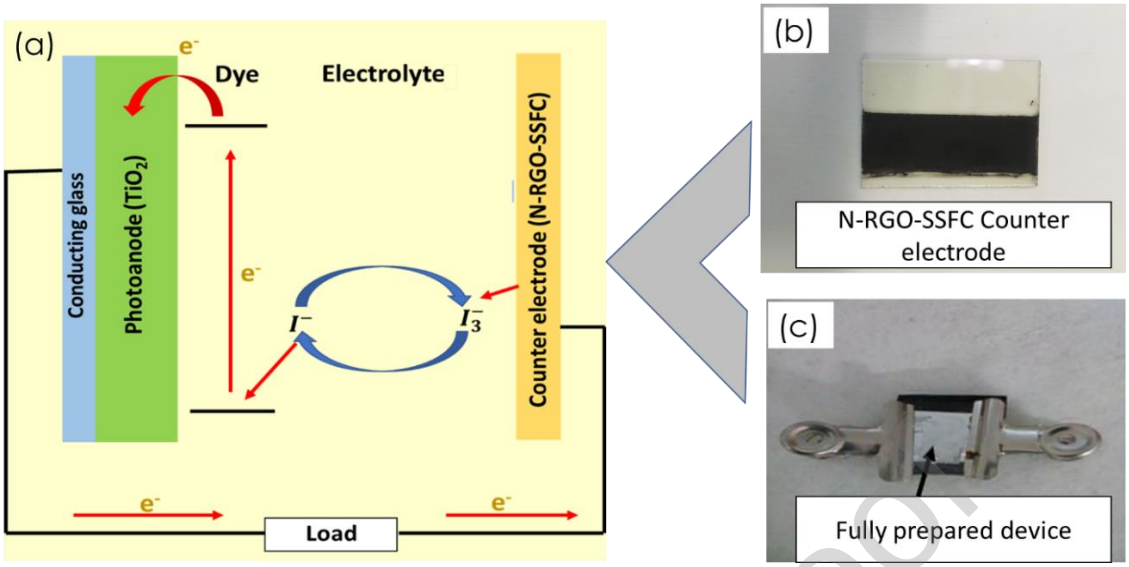

Fig. 1. (a) Schematic diagram of a DSSC, (b) N-RGO-SSFC prepared counter electrode, and (c) the image of a complete fabricated device.

2.7. Characterization

Different phase structures were characterized using a Rigaku Miniflex600 diffractometer, and measurements were recorded in 2θ steps from 20 to 90° using a Cu-Kα radiation source (λ = 0.154 nm). The FullProf program software using the Rietveld refinement technique was used as the software to analyze all the X-ray diffraction (XRD) patterns. The Rietveld method has been used to extract structural details from powder diffraction data. Initially, the main parameters, such as scale factors and background, were refined, followed by the refinement of lattice and width parameters, profile shape, preferred orientation, isothermal parameters, asymmetry, atomic coordinates, and site occupancies were all refined. The fitting quality of various samples' experimental data was assessed by computing the parameters *viz.*, factors (R), Bragg factor (R_B), profile factor (R_P), and crystallographic factor (R_F) and goodness of fit (χ^2) to obtain the best fit in the experimental diffraction data [72]. The microstructural features of the samples were investigated using transmission electron microscopy (TEM JEOL JEM-1010). About 1 mg of the sample was added to a vial and topped with ethanol before sonication for 10 min to form a good dispersion prior to TEM analysis. Different particle sizes of the samples were estimated using the Image J software. The surface morphology was studied using field emission scanning electron microscopy (FE-SEM JEOL JSM-6100, Carl Zeiss Ultra Plus) equipped with energy-dispersive X-ray spectroscopy. Concisely, black carbon tape was glued on top of an aluminium stub sample holder. The sample was coated on carbon tape and further gold-coated under a nitrogen trice before

analysis. Different functional groups in the samples were examined using a Perkin Elmer Spectrum 100 Fourier-transform infrared (FTIR) spectrometer. The crystalline nature of the samples was studied using a DeltaNu Advantage 532^{TM} Raman spectrometer at a wavelength of 515 nm. Prior to analysis, the prepared sample was added into KBr (0.003:0.024 g) and pressed to form a pellet for 5 min at a pressure of 15 Tons. Elemental analysis (CHNS/O) was done using an LEO CHNS-932 elemental analyzer. The surface areas and the porosities of GO, RGO, RGO-SSFC and N-RGO-SSFC were measured using a Micromeritics ASAP 2010 instrument.

The Shimadzu UV-Vis NIR spectrophotometer was used to study the absorbance of samples. The photoluminescence spectra obtained from the PerkinElmer LS 55 spectrometer with a solid format accessory were used to study the charge recombination rate of the samples. The electric conductivity of the prepared samples was investigated using a Keithley 2400 four-point probe source meter by first preparing pellets with a thickness of 0.1 mm from the prepared sample (0.03 g). Cyclic voltammetry (CV) and electrochemical impedance spectroscopy (EIS) were examined using the Metrohm 797 VA Compitrance electrochemical workstation equipped with the ZSimpWin software, at a scan rate of 5 - 100 mV s^{-1} in the potential range from -0.6 to 0.4 V. The electrolyte, reference electrode, counter electrode, and working electrode used herein were potassium hydroxide (KOH) (3 M), Ag/AgCl, Pt, and a mixture of prepared samples, respectively. The working electrode was prepared by casting a mixture of Nafion binder and samples dispersed in absolute ethanol. Photovoltaic characteristics of the prepared DSSCs with an electrode active area (0.92 cm^2) were investigated with a solar simulator (model SS50AAA) using a Keithley HP2400 source meter with a power intensity (100 mW cm^{-2}), operating at AM 1.5 G with a maximum power (750 W), Xenon short AKC lamp (150 W), frequency (50 – 60 Hz), and voltage (116 – 220 V). Prior to the photovoltaic measurements, the working distance (8.90 cm) was calibrated using a standard (high-quality silicon reference cell, Open RR-1002) solar cell sample by adjusting the distance between the standard solar cell and the light source until the PCE of the standard solar cell was determined. All the characterizations were prepared in an ambient laboratory environment.

3 Results and discussion

3.1. Phase composition and structure parameters

Different phase compositions and crystal structures of GO, RGO, SSFC, RGO-SSFC, and N-RGO-SSFC were examined by powder XRD analysis using the Rietveld method (Fig. 2). A strong diffraction peak of GO was observed at 14°, corresponding to the (002) crystal plane. This indicates GO formation from a graphite powder after oxidation using strong acids in Section 2.2. The formation of RGO has been confirmed by the change of crystal planes from (002) for GO to (004) for RGO. However, for RGO-SSFC and N-RGO-SSFC, the peak at 14° was devoured, and this might be related to the removal of oxygen functional groups during thermal treatment. RGO exhibits a strong diffraction peak at 35°, corresponding to the (004) plane. The SSFC nanoparticles had a body-centred tetragonal structure with the I4/mmm space group. The XRD spectrum of SSFC nanoparticles revealed the formation of good crystalline peaks, which indicate the nucleation and growth of the perovskite structure at 600 °C. SSFC, RGO-SSFC, and N-RGO-SSFC exhibited dominant 2θ peaks at 26, 34, 38, 42, 47, 59 and 73°, corresponding to the (100), (110), (111), (200), (211), (220) and (300) crystal planes, respectively, with different primary phases formed as Fe_2O_3, $SrFeO_{2.97}$ and $SrCoO_{2.80}$. The characteristic diffraction peaks of SSFC, RGO-SSFC, and N-RGO-SSFC were sharp, indicating that SSFC has high crystallization and purity. The imperfect nature of peaks in N-RGO-SSFC could be attributed to the dislocations and defects induced on the crystal lattice when doping with nitrogen compared to RGO-SSFC. In addition, the formation of tiny peaks on N-RGO-SSFC could be due to some poor phase separation or distortion that occurred on the crystal lattice during synthesis.

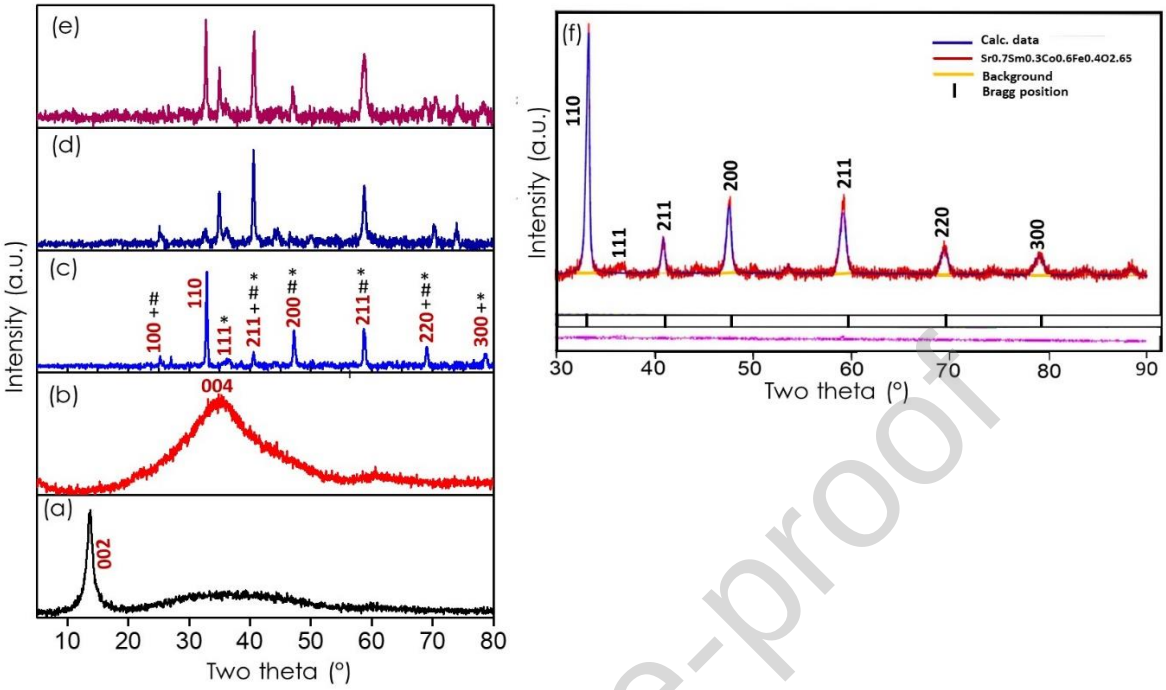

Fig. 2. X-ray diffractograms of (a) GO, (b) RGO, (c) SSFC, (d) RGO-SSFC, and (e) N-RGO-SSFC. (f) Rietveld refined XRD pattern for SSFC. Symbolise denote + Fe_2O_3, # $SrFeO_{2.97}$ and * $SrCoO_{2.80}$.

Table 1. The 2θ, interlayer spacing (d), crystallite sizes (D), and site occupancies values for the samples. D^+ and D* denote the crystallite sizes obtained by the Rietveld method and the Scherrer equation, respectively.

Samples	2θ (°)	d (nm)	D^+ (nm)	D* (nm)	Element site occupancies				
					Sr	Sm	Fe	Co	O
GO	13.9	1.15	-	-	-	-	-	-	-
RGO	33.0	0.80	-	-	-	-	-	-	-
SSFC	32.8	2.25	23.8	24.5	0.701	0.299	0.400	0.600	2.652
RGO-SSFC	32.8	0.23	21.5	24.1	0.704	0.296	0.399	0.601	2.650
N-RGO-SSFC	32.8	0.20	21.0	23.9	0.703	0.297	0.400	0.600	2.651

The Rietveld method from the powder XRD analysis (Section 2.7) was used to confirm the stoichiometries of SSFC, RGO-SSFC, and N-RGO-SSFC, illustrated in Fig. 2. (f). During refinement, the O_2 positions (x = y = z) were set as free parameters; however, all other atomic

fractional positions were fixed. In addition, isothermal parameters, lattice constants, scale factors, shape parameters, and occupancies were taken as free parameters [73]. Initially, the C-file for our structure was $SrCoO_3$ (COD-1551939), which was modified by including additional Sm (in the A-site) and Fe (in the B-site) elements. The obtained structural parameters (see Table 1 and supplementary data Fig. S1), i.e., side occupancy multiplied by multiplicity, were used to elucidate the structural formula as $Sr_{0.7}Sm_{0.3}Fe_{0.4}Co_{0.6}O_{2.65}$ (SSFC). A similar structural formula was also obtained in RGO-SSFC and N-RGO-SSFC to confirm the presence of SSFC in the nanocomposites. Similar findings were also observed by Sithole et al. [74].

In Table 1, interlayer spacing (d) was calculated using 2θ angles, and the crystallite sizes (D) were calculated using the Scherrer equation (Equation 1) and Rietveld method (Equation 2) [72]:

$$D = \frac{k\lambda}{\beta \cos\theta} \qquad (1)$$

where k, λ, β, and θ denote the shape factor (0.9), X-ray wavelength (1.541 Å), full width at half maximum (FWHM), and the diffraction angle, respectively.

$$FWHM^2 = (U + D_{ST}^2)(\tan\theta) + V(tan^2\theta) + W + \frac{IG}{cos^2\theta} \qquad (2)$$

where U, V, and W denote the peak shape parameters, D_{ST} measures the coefficient related to strain, and IG is the isotropic size effect. The interlayer spacing of N-RGO-SSFC was calculated and found to be 0.20 nm, which is smaller than the calculated 1.15 nm for GO. The decrease in interlayer spacing was attributed to the reduction of oxygen functional groups, such as hydroxyl, epoxy, and carboxyl, as revealed in Fig. 2, by the change from the (001) to the (004) crystal plane. SSFC, RGO-SSFC, and N-RGO-SSFC crystallite sizes were calculated using the Scherrer equation as 24.4, 24.6, and 23.9 nm, respectively. On the other hand, the crystallite sizes of SSFC, RGO-SSFC, and N-RGO-SSFC calculated using the Rietveld method were found to be 23.8, 21.5, and 21.0 nm, respectively. The crystallite sizes determined using the Rietveld method were noted to be smaller than those obtained using the Scherrer equation by ~1 to 2% due to the correction of peak broadening, taking into account all various instrumental factors found in the Rietveld method. The small crystallite sizes obtained for N-RGO-SSFC by both methods could be beneficial in forming a high surface area, which is vital for creating more catalytic active sites.

3.2. Microstructure and surface morphology

The microstructure and surface morphology of GO, RGO, SSFC, RGO-SSFC, and N-RGO-SSFC were investigated using TEM and FESEM images, as shown in Fig. 3 and 4, respectively. In Fig. 3 (a), the image of GO shows a wrinkled structure, which reveals the edges to be folded and scrolled slightly due to the presence of oxygen functional groups. Fig. 3 (b) reveals the exfoliated sheets of RGO. Fig. 3 (c) shows the distribution of agglomerated SSFC nanoparticles. Fig. 3 (d) reveals the RGO decorated by SSFC nanoparticles. The N-RGO-SSFC image in Fig. 3 (e) shows a more wrinkled structure due to the reduction of GO, doping with nitrogen dopants, and the introduction of SSFC nanoparticles. The wrinkles formation could be caused by the stimulation of defects, such as cavities, holes, and pores, that occur during doping with nitrogen [75]. In Fig. 3 (e), the uniform distribution of spherical particles and an irregular net-like structure of SSFC with less agglomeration were observed to be anchored on the N-RGO basal plane. When SSFC was deposited on the RGO surface, the resulting N-RGO-SSFC exhibited morphologies corresponding to the SSFC nanoparticles and N-RGO sheets, as shown in Fig. 3 (d). After reduction, the SSFC nanoparticles might have interacted with the sheet surface through the remaining carbon atoms and the carboxyl and hydroxyl groups, which can be attributed to self-assembly growth to form the covalent bond [76]. The average particle sizes of SSFC, RGO-SSFC, and N-RGO-SSFC were calculated to be 24.2, 24.7, and 23.4 nm, which was comparable to the XRD results obtained in Table 1.

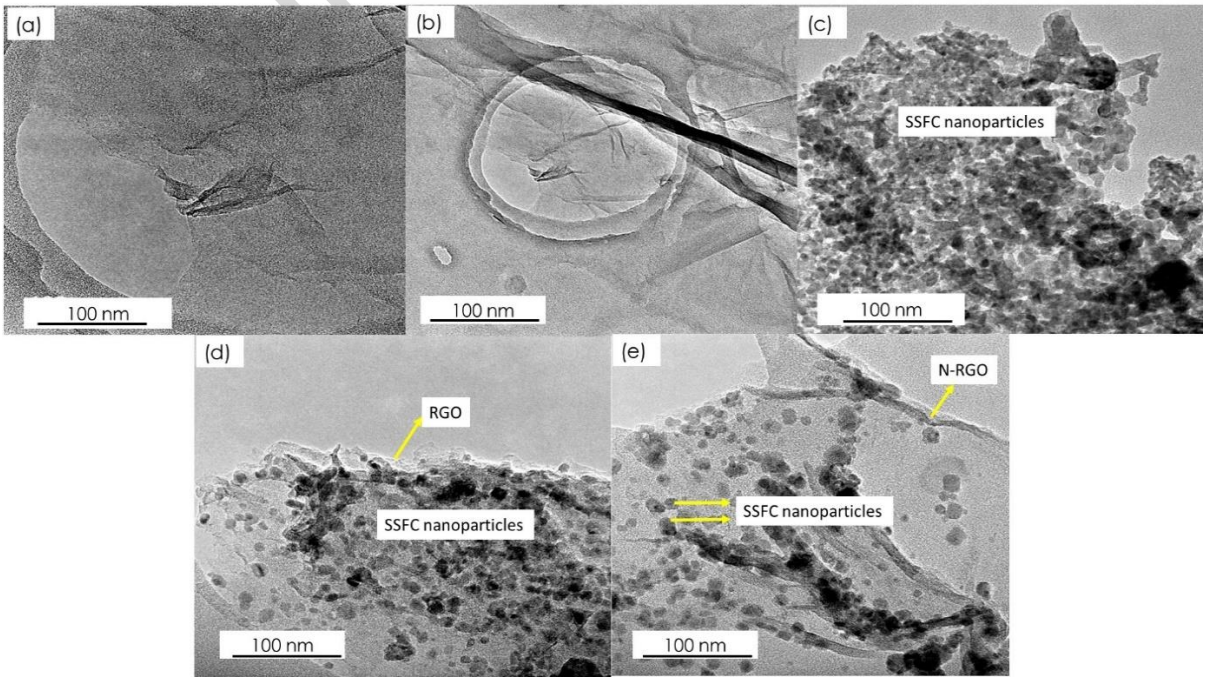

Fig. 3. TEM images of (a) GO, (b) RGO, (c) SSFC, (d) RGO-SSFC, and (e) N-RGO-SSFC nanocomposite.

The SEM image in Fig. 4 (a) shows GO formation with wrinkles due to oxygenated functional groups. Fig. 4 (b) shows the exfoliated RGO sheets, which reveals the successful reduction of GO. Fig 4. (c) reveals the distribution of SSFC nanoparticles. Fig. 4 (d) and (e) show the SSFC nanoparticles distributed on RGO and N-RGO sheets with less agglomeration and few layers, which could contribute to efficient electron transport and light harvesting. All SEM images (Fig. 4 (a - e)) strongly agree with the findings obtained in Fig. 3. EDX analysis coupled with FESEM was used for qualitative analysis to measure the elemental compositions of various prepared samples. EDX spectrum and elemental mapping analyses of the N-RGO-SSFC nanocomposite are presented in Fig. 4 (f). The corresponding elements, *viz*., C, Sr, Sm, Fe, Co, and O, present on the nanocomposite, were uniformly distributed throughout the sample on the SEM mapping image. However, the nitrogen content was poorly detected by EDX mapping; hence, it was further analyzed using elemental analysis.

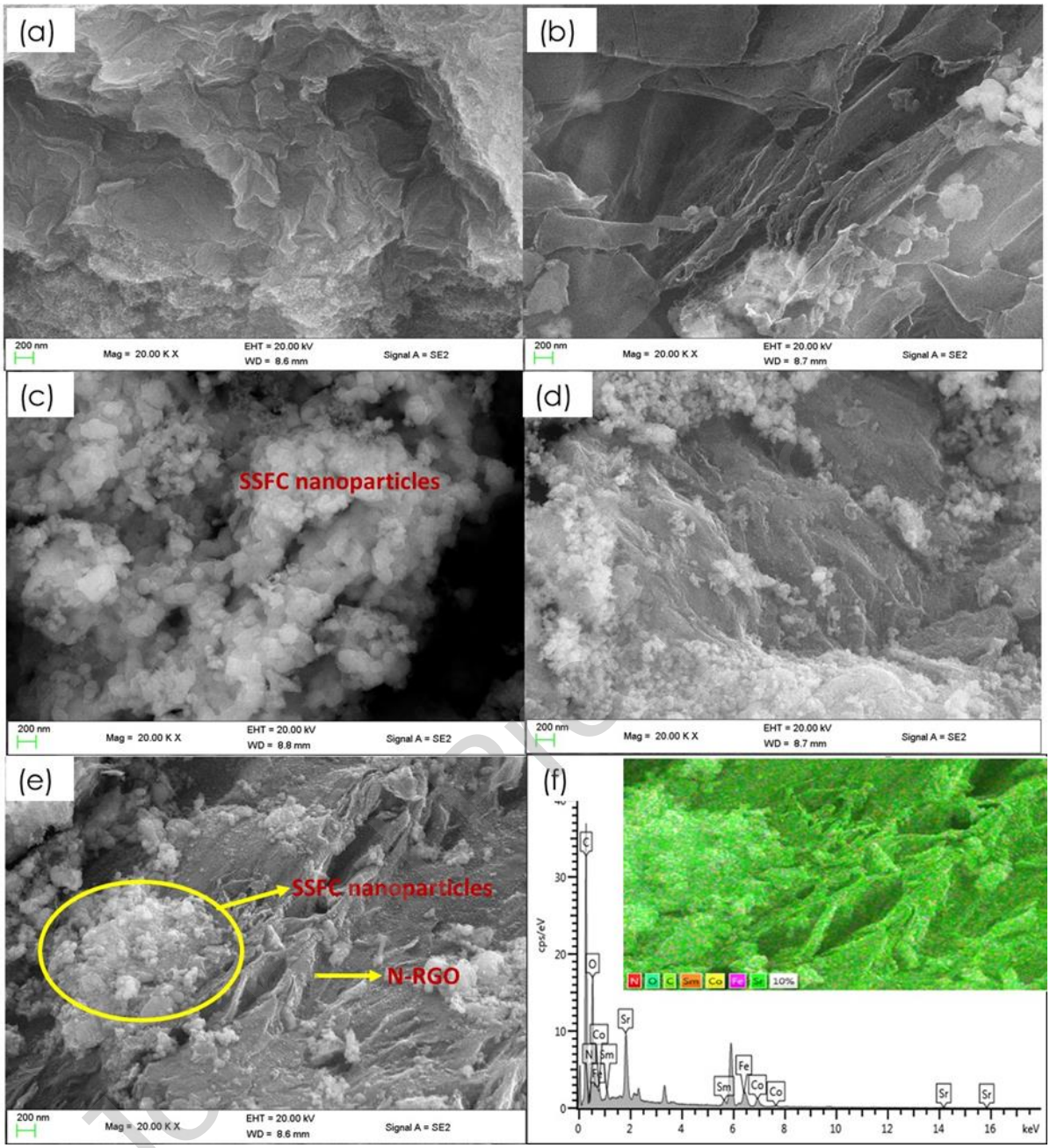

Fig. 4. SEM images of (a) GO, (b) RGO, (c) SSFC, (d) RGO-SSFC, and (e) N-RGO-SSFC. (f) EDX spectrum of the N-RGO-SSFC nanocomposite. Inset denotes elemental mapping.

3.3. Carbon, hydrogen, nitrogen, and oxygen (CHNO) content

Elemental analysis (CHNO) was employed to study the elemental composition of the samples, and the results are shown in Table 2. The elemental analysis of SSFC reveals the presence of O, without H and C. The amount of O was not much because the remaining percentages were for metals (Sr, Sm, Fe, or Co), which indicates that SSFC was formed. The other metal elements, such as Sr, Sm, Fe, and Co, were identified using the EDX spectrum in Fig. 4. GO revealed the presence of C, H, and O. This showed high content of oxygenated groups that

were present after oxidation, which correlates with the findings for XRD in Fig. 2. The presence of oxygen moieties, such as -OH, -COOH and -C-O-C, on GO could be attributed to the oxidation of graphite done using a strong oxidizing agent, such as concentrated H_2SO_4 used in Section 2.2. RGO reveals a decrease in oxygenated functional groups from 40.52% for GO to 25.06% for RGO, indicating the successful reduction of oxygenated functional groups. The introduction of SSFC onto RGO was noted to decrease the content of oxygen from 25.06% for RGO to 10.26 % for RGO-SSFC, probably due to the binding of SSFC nanoparticles (Sr^{2+}, Sm^{3+}, Fe^{3+} or Co^{3+}) onto the remaining oxygen functional groups after reducing GO to form RGO. The N-RGO-SSFC revealed the presence of C, H, O, and N elements. The presence of N on NRGO-SSFC could be attributed to the nitrogen-containing functional groups that occur during nitrogen-doping.

Table 2. Elemental and EDX analysis of GO, RGO, SSFC, RGO-SSF, and N-RGO-SSFC.

Samples	Elemental analysis			
	C (%)	H (%)	O (%)	N (%)
GO	58.6 ± 0.06	0.86 ± 0.05	40.52 ± 0.08	-
RGO	74.5 ± 0.07	0.43 ± 0.08	25.06 ± 0.07	-
SSFC	-	-	20.62 ± 0.06	-
RGO-SSFC	48.9 ± 0.06	1.09 ± 0.03	10.26 ± 0.04	-
N-RGO-SSFC	37.4 ± 0.03	0.96 ± 0.05	11.68 ± 0.07	10.06 ± 0.02
	EDX analysis			
	Sr (%)	Sm (%)	Fe (%)	Co (%)
GO	-	-	-	-
RGO	-	-	-	-
SSFC	28.69 ± 4.96	21.80 ± 5.03	10.93 ± 4.52	17.91 ± 2.96
RGO-SSFC	14.85 ± 5.06	10.97 ± 3.75	5.42 ± 2.46	8.56 ± 3.16
N-RGO-SSFC	14.61 ± 5.42	11.26 ± 3.12	5.56 ± 2.87	8.39 ± 4.12

3.4. Surface functional groups

The formation of SSFC perovskite and the introduction of SSFC onto RGO was confirmed using FTIR analysis. Different functional groups present in GO, RGO, SSFC, RGO-SSFC, and N-RGO-SSFC are shown on the FTIR spectra in Fig. 5. In Fig. 5 (a), GO shows the presence of different functional groups, such as -OH, C=O, aromatic C=C, and C-O, at 3400,

1640, 1490 and 1080 cm^{-1} stretching, respectively. In Fig. 5 (b), the RGO spectrum reveals a decrease in the number of oxygenated function groups due to the reduction of GO to RGO, as supported by elemental analysis in Table 2. The remaining oxygen functional groups, such as -OH, might facilitate the self-assembly of nitrogen atoms and bind with metals (Sr, Sm, Fe, and Co) to possibly form a covalent bond with RGO sheets [76,77]. The SSFC spectrum revealed the formation of perovskite dominant peaks, such as Fe-O, Co-O, Sr-O-Sm, and O-H, at about 500, 590, 800, and 1450 cm^{-1}, respectively. SSFC peaks were also noted on the RGO-SSFC and N-RGO-SSFC spectra, probably due to the binding of SSFC metals onto RGO sheets. RGO-SSFC and N-RGO-SFFC reveal the formation of a new C-O-M peak (where M symbolizes Sr, Sm, Fe, or Co) at 1094 cm^{-1}. The new peak could have originated from the strong synergistic effect between SSFC nanoparticles and RGO sheets, which signifies the incorporation of SSFC onto RGO or N-RGO layers. Furthermore, the N-RGO-SSFC peak at 1296 cm^{-1} represented the C=N bending vibration, which reveals the doping of nitrogen dopants onto RGO-SSFC [78]. This could be observed through peak overlapping hybridization between nitrogen and carbon atoms, which does not allow changes in the dipole moment.

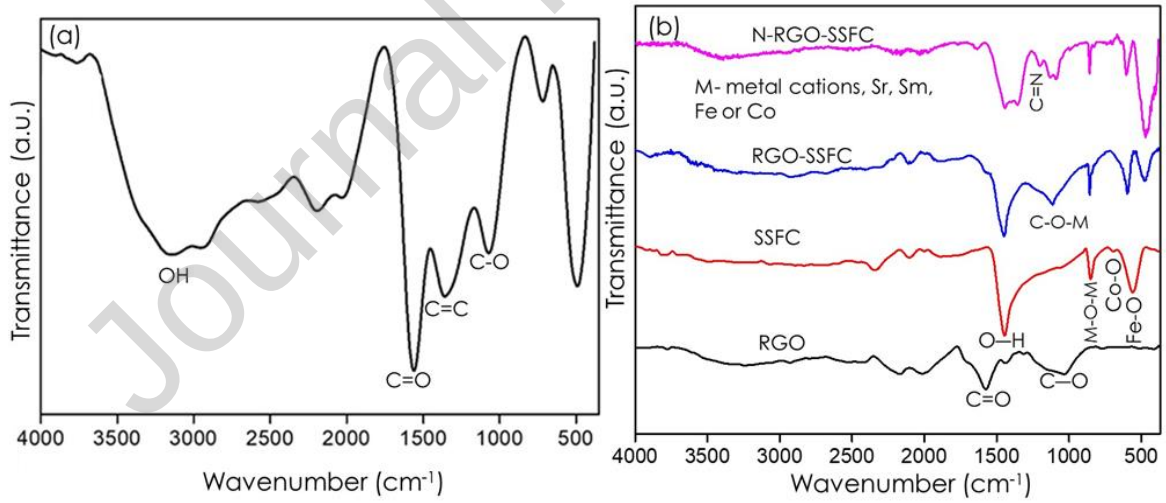

Fig. 5. FTIR spectra of (a) GO and (b) RGO, SSFC, RGO-SSFC and N-RGO-SSFC.

3.5. Defects on the graphitic structure

Raman analysis was used to investigate the electronic properties and structural information, such as the defect state and graphitic nature of GO, RGO, RGO-SSFC, and N-RGO-SSFC. It was further used to investigate the extent of disorders created by N-doping onto RGO-SSFC. The formation of SSFC perovskites was confirmed by the presence of the dominant peak at

around 800 cm^{-1}, Fig. 6 (a), which signifies the asymmetric stretching of M-O-M, where M symbolizes Sr, Sm, Co, or Fe. A similar peak at 800 cm^{-1} was also observed for RGO-SSFC and N-RGO-SSFC, confirming SSFC perovskites on the nanocomposite. In this way, perovskite metals *viz.*, Sr^{2+}, Sm^{3+}, Fe^{3+}, or Co^{3+}, probably would interact with the highly electronegative exfoliated GO during thermal treatment, while GO is reduced to RGO, which is hydrophobic due to the weakening of π-π interactions in the RGO sheets.

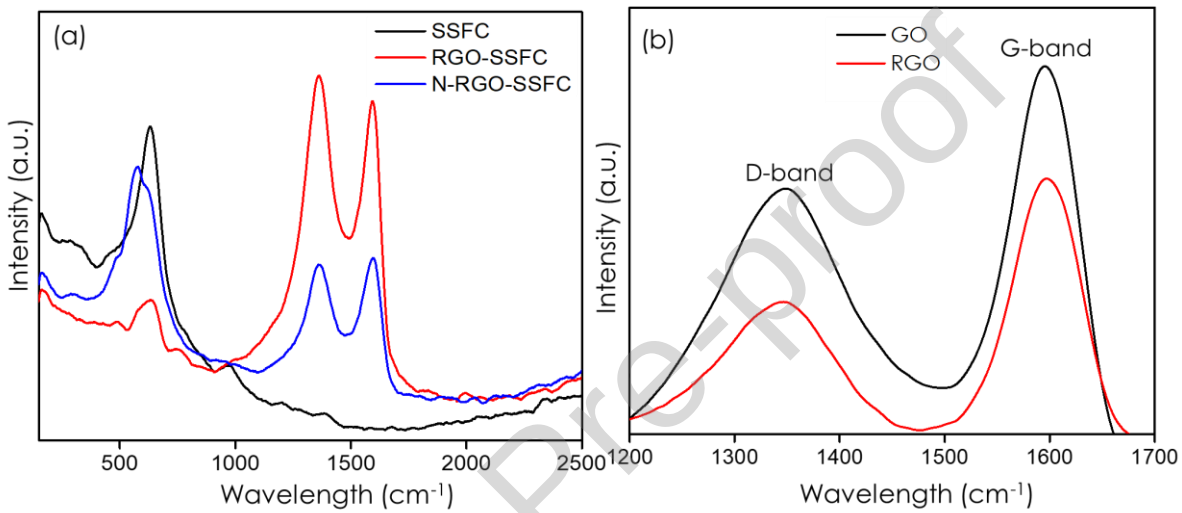

Fig. 6. Raman spectra of (a) SSFC, RGO-SSFC, and N-RGO-SSFC and (b) GO and RGO.

Fig. 6 (a) and (b) show two dominant peaks for the D- and G-bands that appeared at 1350 and 1550 cm^{-1}, respectively. The D band peak is associated with disorder and defects, whereas the G band is associated with the stretching vibration of the E_{2g} mode on the sp^2 carbon lattice [79,80]. The I_D/I_G ratio of the materials was calculated and presented in Table 3. The I_D/I_G ratio of GO was 0.90, which indicates the formation of high sp^2-hybridized C-C domains on the layer. The I_D/I_G ratio of RGO was 0.72, which indicates the removal of oxygenated functional groups on RGO sheets and the regaining of sp^2-hybridized C-C bonds. However, the I_D/I_G ratio of RGO-SSFC (1.04) was higher than that of GO due to the decrease in sp^2-hybridized C-C domains and the introduction of SSFC nanoparticles onto RGO sheets on the radicalized RGO sites, which introduces defect active sites on RGO sheets. The highest I_D/I_G ratio of N-RGO-SSFC (1.20) indicates the presence of residual oxygen, which binds the introduced SSFC nanoparticles, resulting in structural defects on the RGO sheet upon doping with nitrogen. A similar observation was reported by Yang et al. [69], whereby $La_{0.7}Ca_{0.3}MnO_3$ nanoparticles anchored on the surface of N-doped graphene, and the

introduction of SSFC and nitrogen doping caused structural aberration. Thus, nitrogen doping for RGO could induce structural defects due to the variation in bond distance between C-N and C-C. The defect-active sites are beneficial for catalysis, stabilizing nanoparticles, and molecular attachments.

Table 3. Raman data of GO, RGO, RGO-SSFC, and N-RGO-SSFC.

Samples	D-band (cm^{-1})	G-band (cm^{-1})	I_D/I_G
GO	1350	1593	0.90
RGO	1348	1600	0.72
SSFC	-	-	-
RGO-SSFC	1346	1601	1.04
N-RGO-SSFC	1345	1603	1.20

3.6. Surface area and porosity

The nitrogen adsorption-desorption isotherms used to measure the surface area and porosity of SSFC, GO, RGO, RGO-SSFC, and N-RGO-SSFC were obtained from Brunauer-Emmett-Teller (BET) analysis, and are shown in Fig. 7. In Table 4, all synthesized samples exhibited different surface areas, pore volumes, and sizes. SSFC was observed to have a surface area of 52.4 $m^2 g^{-1}$. GO exhibited the lowest surface area of 48.1 $m^2 g^{-1}$, which could be correlated to strong hydrogen bonds forming agglomerated sheets, as observed in Fig. 4 (a). The obtained surface area of GO is consistent with the one reported in the literature [81]. RGO exhibited a higher surface area of 95.6 $m^2 g^{-1}$ when compared with GO, due to the reduction of oxygenated functional groups, as correlated with FTIR in Fig. 5. Similar findings for RGO were observed by Chakrabarty et al. [82].

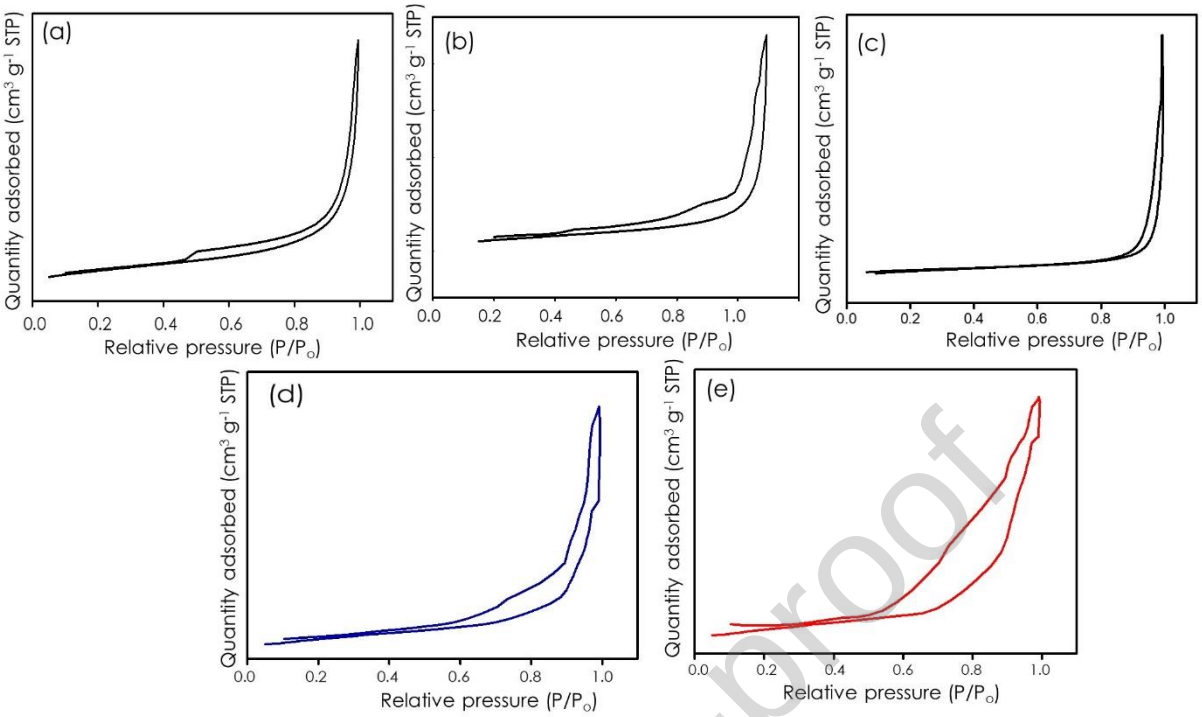

Fig. 7. Nitrogen adsorption-desorption isotherms of (a) GO, (b) RGO, (c) SSFC, (d) RGO-SSFC, and (e) N-RGO-SSFC.

The surface areas of RGO-SSFC and N-RGO-SSFC were noted to be 140.3 and 178.0 $m^2 g^{-1}$, respectively. This was influenced by the presence of SSFC on RGO, which induced the restacking, disorientation, and corrugation of graphitic basal planes. The increase in surface area and pore volume of N-RGO-SSFC leads to the creation of more active sites due to the presence of defects, as shown in Table 3. This facilitates faster dye regeneration due to elevated electron transport, thus resulting in superior electrochemical properties and electrical conductivity. Fig. 7 reveals the type IV isotherms with the possibility of an H3 hysteresis loop due to capillary condensation. Compared to RGO-SSFC, N-RGO-SSFC reveals a larger hysteresis loop, indicating a larger surface area and pore volume formation. The pore size distribution was found to be in the range of 2 - 10 nm, which indicates the mesoporous structure of the prepared samples [83]. The formation of mesopores is beneficial for inserting and deinsertion ions during charging and discharging processes, improving the electrochemical properties.

Table 4. Surface area and porosity of the GO, RGO, SSFC, RGO-SSFC, and N-RGO-SSFC.

Samples	Surface area ($m^2 g^{-1}$)	Pore volume ($cm^3 g^{-1}$)	Pore size (nm)

SSFC	52.4	0.332	2.82
GO	48.1	0.065	3.69
RGO	95.6	0.869	5.40
RGO-SSFC	144.6	1.028	7.96
N-RGO-SSFC	179.8	1.865	9.28

3.7. Optoelectronic transition studies

Ultraviolet-visible (UV-Vis) spectroscopy was used to study the optical properties and energy bandgaps of GO, RGO, SSFC, RGO-SSFC, and N-RGO-SSFC, as shown in Fig. 8. The SSFC was strongly absorbing in the wavelength range of 250 - 310 nm, as revealed in Fig. 8 (a). This implies that SSFC absorbs at the ultraviolet region. The GO, RGO, RGO-SSFC, and N-RGO-SSFC were absorbed in the 300 - 500 nm wavelength range due to the $\pi \rightarrow \pi^*$ transitions, as shown in Fig. 8 (b). This indicates that GO, RGO, RGO-SSFC, and N-RGO-SSFC absorb light in the visible range.

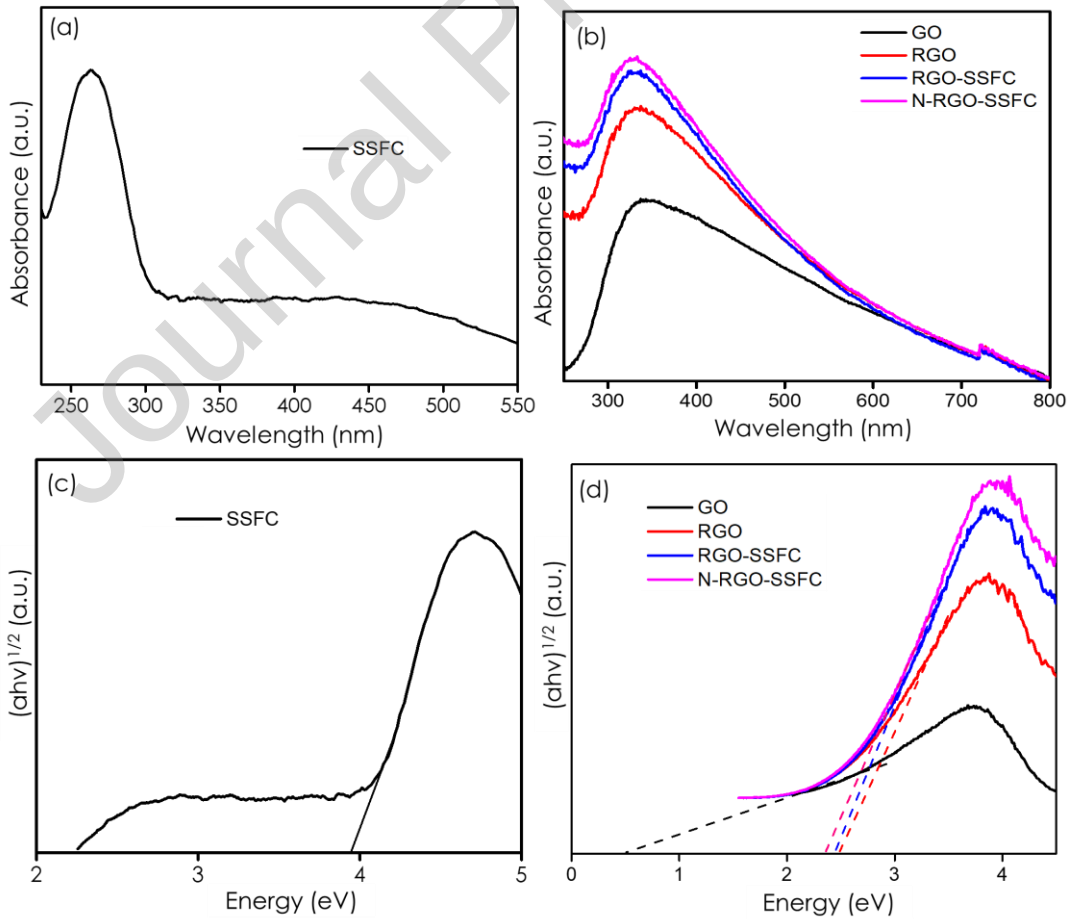

Fig. 8. UV-Vis absorption spectra of (a) SSFC and (b) GO, RGO, RGO-SSFC, and N-RGO-SSFC. Tauc plots for (c) SSFC, and (d) RGO, RGO-SSFC, and N-RGO-SSFC.

The energy bandgaps of the prepared samples were obtained from the Tauc plots, shown in Fig. 8 (c) and (d). The calculated energy bandgaps for SSFC, RGO, RGO-SSFC, and N-RGO-SSFC were found to be 3.9, 0.4, 2.5, 2.4, and 2.3 eV, respectively. Among these, GO exhibited the smallest energy bandgap of 0.4 eV since GO is known to possess a zero energy bandgap due to its conduction band, which allows contact with the Dirac point at the valence band, thereby allowing GO to function as a semimetal [84]. These findings correlate with the work of Ngidi et al. [85], who obtained graphene-based materials with energy bandgaps in the 1.3 – 3.4 eV range. The N-RGO-SSFC energy bandgap was found to be 2.3 eV, due to the reduction in oxygenated functional groups. Also, introducing nitrogen atoms onto RGO-SSFC allows the Fermi level to move near the Dirac point to suppress the nearby density of states [86]. This results in a band opening and shift between the conduction and valence bands. The lower bandgap could be beneficial for transporting and collecting electrons in solar energy harvesting.

3.8. Electron-hole transition studies

The recombination rate between photoinduced electrons and photogenerated holes of the prepared samples was investigated using photoluminescence spectroscopy (PL). Fig. 9 (a). reveals the major charge transport and transfer processes in a DSSC device. The arrows 2, 5, 6, and 7 involve electron transfer, and arrows 3, 4, and 8 show the lost reactions [87]. Upon illumination, the dye/harvester molecules absorb light, the dye gets excited (arrow 1), and the ultrafast electrons are injected into the TiO_2 conduction band (arrow 2). On the DSSC device, two major backreactions normally occur: the recombination of an oxidized dye molecule with TiO_2 conduction band electrons (arrow 3) and the recombination of TiO_2 conduction band electrons with an iodine electrolyte (arrow 4) [87]. The direct recombination (arrow 8) of the excited dye is reflected by an excited state lifetime. Hence, the electrons are transported into the TiO_2 semiconductor to the back contact (arrow 5). The reduction rate of an oxidized dye (D^+) occurs very fast, which can compete with the backreaction (arrow 3) to allow the collection of photoelectrons by the back contact. Furthermore, I^- is regenerated (arrow 6) in turn by the reduction of I_3^- electrons that pass through the external circuit.

Fig. 9 (b) and (c) show the PL spectra of various prepared materials. The SSFC spectrum exhibits a peak in the 590 – 630 nm range with the highest intensity of 0 - 780 a.u., which symbolizes a high charge recombination rate, as shown in Fig. 9 (a). The RGO-SSFC and N-RGO-SSFC spectra show a peak in the 660 – 710 nm range with an intensity of 0 – 100 a.u. The RGO-SSFC and N-RGO-SSFC nanocomposites reveal quenching of the PL intensity when compared to GO and RGO. This allows for better electron transportation and collection due to low charge recombination at the counter electrode. This could be attributed to the introduction of energy states/extra traps within the CB and VB of the nanocomposites, resulting in reduced charge carrier recombination, thereby increasing the performance of the device. Thus, N-RGO-SSFC can assist in minimizing recombination reactions during electron transfer between the electrolyte and counter electrode [88].

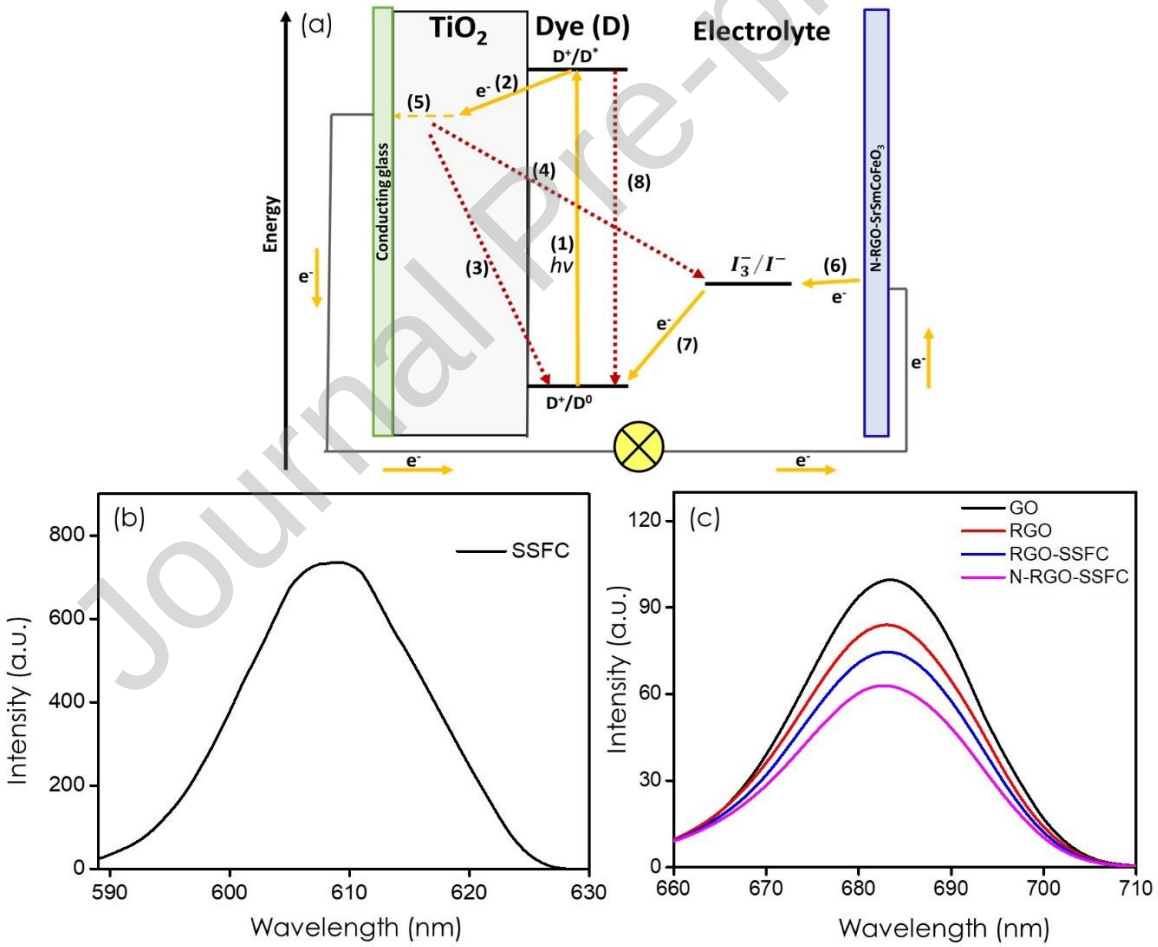

Fig. 9. (a) The basic charge transport processes. The photoluminescence spectra of the (b) SSFC and (c) GO, RGO, RGO-SSFC and N-RGO-SSFC.

3.9. I-V characteristics

Four-point probe measurements were used to investigate the electrical resistivity and conductivity of GO, RGO, SSFC, RGO-SSFC, and N-RGO-SSFC. The electrical conductivity parameters and current-voltage (I-V) curves of SSFC, GO, RGO, RGO-SSFC, and N-RGO-SSFC are illustrated in Table 5 and Fig. 10, respectively. The electrical conductivity of the prepared samples was investigated using a Keithley 2400 four-point probe source meter by first preparing pellets with a thickness of 0.1 mm from the prepared sample (0.03 g). The resistivity (ρ) of the prepared samples was calculated using Equation 3:

$$\rho = \left(\frac{\pi}{In2}\right)\left(\frac{V}{I}\right)t \qquad (3)$$

where *V*, *I*, and *t* are the voltage, current, and sheet thickness, respectively. The I-V curve of GO reveals a small slope that is close to zero with an electrical conductivity of 1.24×10^{-5} S cm^{-1}. The poor electrical conductivity could be attributed to GO since it is an insulator due to the structural disorder caused by the C-O bonds on sp^3, which ultimately disrupts its conductive π-network and disrupts the flow of charge carriers and the sp^2 bond network [89]. The disruption can result in low electrical conductivity of GO, which can be improved by reducing GO to form RGO to reduce the presence of the oxygenated functional group. RGO was noted to have a better electrical conductivity of 5.10 S cm^{-1} when compared with 1.24×10^{-5} S cm^{-1} for GO.

Table 5. Electrical conductivity parameters of various prepared samples.

Samples	Resistivity (Ω cm)	Conductivity (S cm^{-1})
GO	80257	1.24×10^{-5}
SSFC	0.4525	2.21
RGO	0.1958	5.10
RGO-SSFC	0.1320	7.57
N-RGO-SSFC	0.0768	13.02

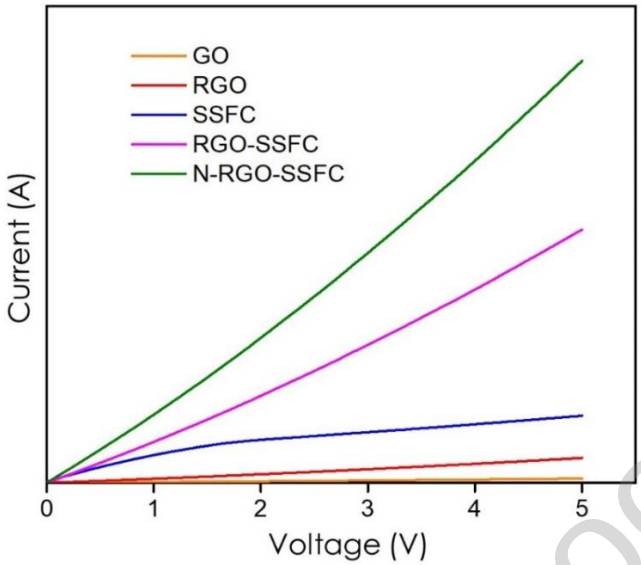

Fig. 10. I-V curves of SSFC, GO, RGO, RGO-SSFC, and N-RGO-SSFC.

SSFC displays a curved I-V graph, revealing its relatively improved resistance. RGO-SSFC and N-RGO-SSFC exhibited nearly linear I-V curves due to their superior electrical resistances. The enhancement of electrical conductivity of the nanocomposites could have originated from the strong synergistic interaction between SSFC and RGO sheet, as observed in Fig. 5. In this way, SSFC nanoparticles can play a huge role by preventing the agglomeration and restacking of RGO sheets, due to van der Waals interactions [90]. Thus, it allows SSFC nanoparticles to act as agents while forming an interconnected conductive porous structure, enhancing electrical conductivity. The improved electrical conductivity of the nanocomposites could also be associated with the strong interaction produced by the coexistence of four metals, such as Sr^{2+}, Sm^{3+}, $Fe^{3+,}$ and Co^{3+}, on the perovskite and RGO, which can transfer charges easily between the electrolyte and counter electrode in DSSC.

The electrical conductivity of the prepared samples was found to increase with the increase in the surface area (see Table 4). The lowest conductivity of GO resulted in a decrease in surface area (see Table 4), probably due to the π-π interaction that resulted in the agglomerated layer. On the other side, the recovery of π-π conjugated structure on the RGO, RGO-SSFC, and N-RGO-SSFC did increase the surface area. Also, the doping of N onto RGO-SSFC might contribute to the formation of more electrons or holes with respect to the valence band of the RGO sheet, which would increase the charge carrier concentration through distortion caused by the nitrogen atom, resulting in the highest electrical conductivity.

3.10. Electrode potential characteristics

The electrochemical properties of GO, RGO, SSFC, RGO-SSFC, and N-RGO-SSFC were investigated using cyclic voltammograms (CV) obtained at a potential window of -0.6 to 0.4 V and a scan rate of 100 mV s^{-1} as shown in Fig. 11. The CV curve, Fig. 11 (a), SSFC exhibited pseudocapacitive characteristics related to Faradaic reactions that occur at the electrode surface [91]. GO, RGO, RGO-SSFC, and N-RGO-SSFC, Fig. 11 (b) to (e), revealed the quasi-rectangular curve. This indicates the redox behaviour with some portion of capacitance. GO showed a smaller quasi-rectangular curve when compared to N-RGO-SSFC, due to the presence of oxygenated functional groups that lower the graphitisation degree of GO, leading to poor electrical conductivity. The reduction of oxygenated functional groups from GO to RGO using thermal treatment, Section 2.2, might contribute to the reduction of surface wetting between electrolyte and electrode by improving the electrical conductivity and capacitance.

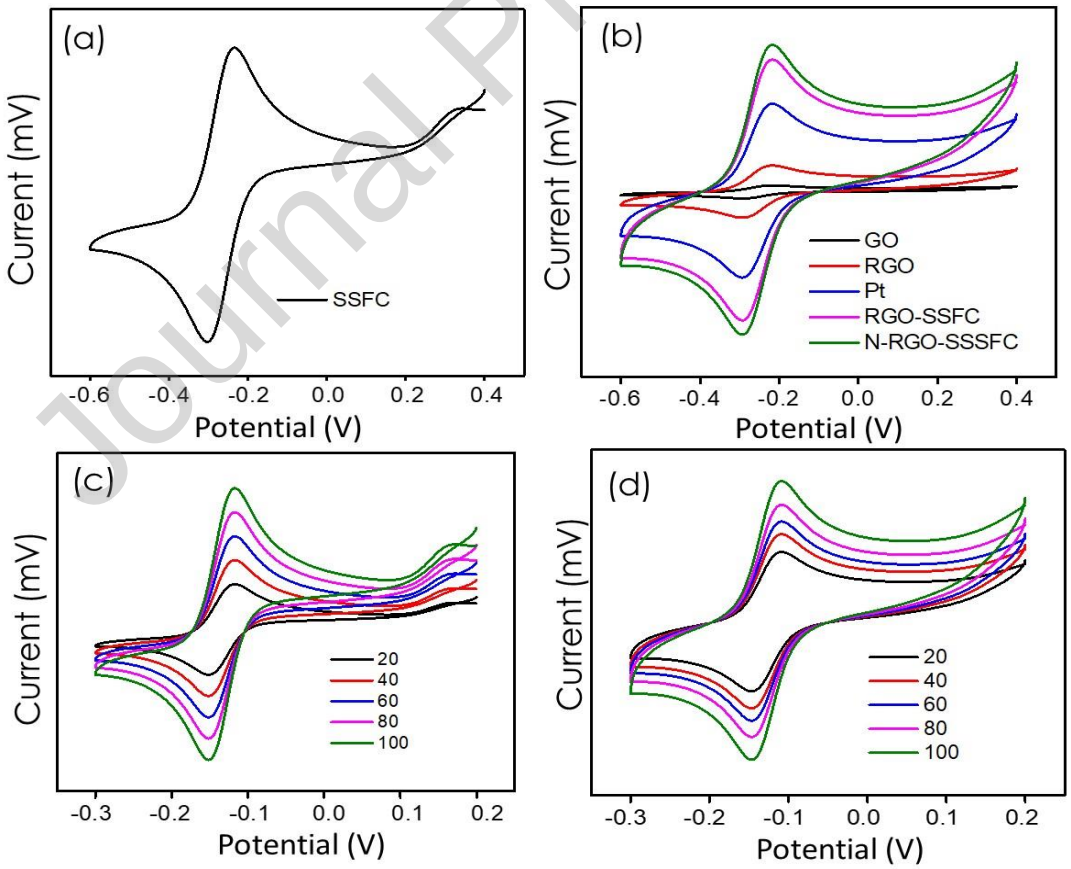

Fig. 11. Cyclic voltammograms of (a) SSFC and (b) GO, RGO, RGO-SSFC and N-RGO-SSFC.

The N-RGO-SSFC nanocomposite exhibited a larger quasi-rectangular curve (Fig. 11 (e)) than other prepared samples due to the SSFC nanoparticles anchored on the N-RGO sheets. This resulted in improving charge response characteristics to facilitate the redox reaction. The chemical coupling between N-RGO and SSFC prevents the aggregation of SSFC nanoparticles on the N-RGO sheet surface and increases charge response, thus leading to a larger contact area with the electrolyte. N-RGO-SSFC showed superior performance, probably due to the higher forms of active ions that lead to faster charge transportation as well as better storage capability. The significant decrease in the resistivity of the N-RGO-SSFC electrode did contribute to the increase of electrical conductivity and charge transfer rate.

3.11. Interfacial charge transfer characteristics

Electrochemical impedance spectroscopy (EIS) is a valuable instrument to elucidate the electrochemical properties of the prepared samples. Electrochemical behaviour was used to examine the prepared samples' charge transfer rate and series resistance when used as electrodes, as shown on the Nyquist plots in Fig. 12. GO electrodes showed a semicircle in the high-frequency region, indicating the electron transfer limiting process, while at the low frequency, the linear part shows the diffusion-controlled process [92]. RGO revealed a smaller semicircle than GO due to the less charge transfer (R_{ct}) from 40.9 to 28.5 Ω, respectively, which improves an electron transfer from the RGO electrode to the interface of the electrolyte. RGO-SSFC and N-RGO-SSFC exhibited a straight line with R_{ct} values of 19.7 and 10.6 Ω, respectively, which signifies an ideal capacitive performance with superior electrical conductivity, Fig. 10, due to high charge transportation characteristics. The R_{ct} values were obtained in decreasing order as 40.9, 28.5, 19.7, and 10.6 Ω for GO, RGO, RGO-SSFC, and N-RGO-SSFC, respectively, signifying the superior electrocatalytic activity of electrolyte when N-RGO-SSFC used as the electrode. The presence of SSFC nanoparticles with R_{ct} of 32.4 Ω onto RGO would play a significant role by preventing the aggregation and restacking of RGO sheets due to van der Waals interactions and enhancing the acceleration of ion transport within the electrode. In addition, the interconnected conductive SSFC network provided an electron transfer channel on the RGO sheet, which significantly enhanced the electrochemical properties [91]. Compared to RGO-SSFC, N-RGO-SSFC as an electrode facilitates the efficient transportation of electrolyte ions throughout the inner surface of the electrode due to lower R_{ct}. The doping of N onto RGO-SSFC can produce local

strains on the hexagonal carbon lattice, which would cause structural deformations by bringing additional lone pair electrons to the sp^2 hybridized carbon framework, thus enhancing electron-transfer ability.

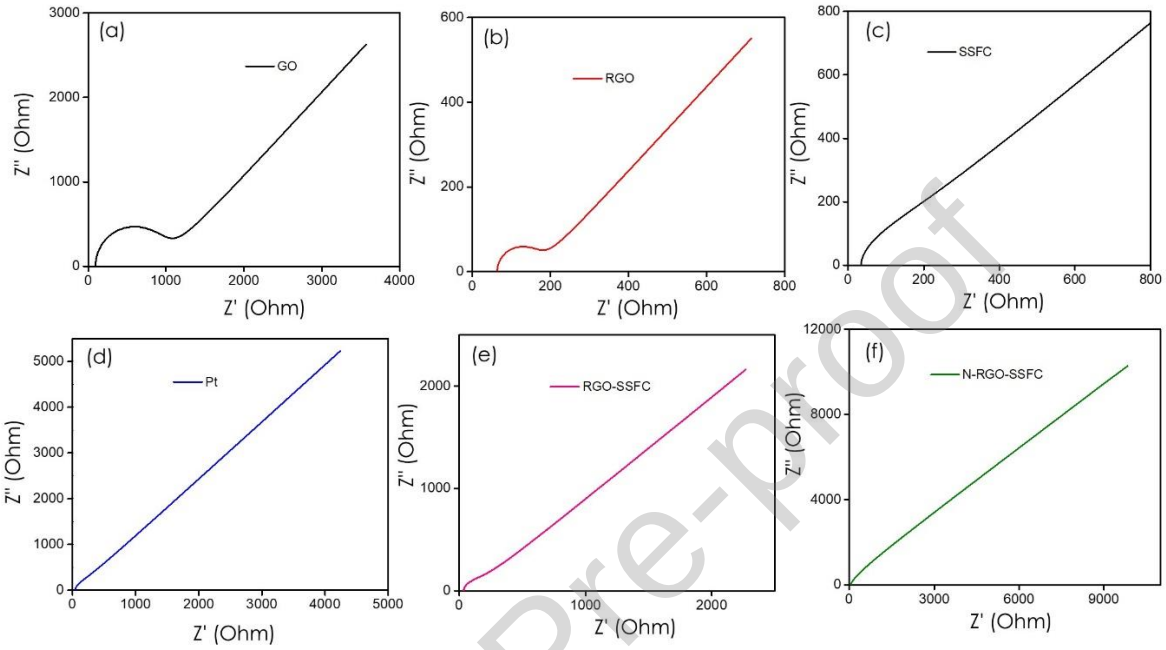

Fig. 12. Nyquist plots for (a) GO, (b) RGO, (c) SSFC, (d) Pt, (e) RGO-SSFC, and (f) N-RGO-SSFC.

3.12. Photovoltaic performance of the fabricated DSSCs

The photovoltaic performance of various prepared samples was studied using the current-voltage characteristics measurements. Differently prepared samples, *viz*., Pt, GO, RGO, SSFC, RGO-SSFC, and N-RGO-SSFC, were used to fabricate the counter electrode, and the corresponding photocurrent density-voltage (J-V) curves for the resulting DSSCs are presented in Fig. 13. The photovoltaic parameters, such as open-circuit voltage (V_{oc}), short-circuit current density (J_{sc}), fill factor (FF) and PCE, for DSSCs using various counter electrodes are summarised in Table 6. The PCE parameters were calculated using Equation 4:

$$PCE = \frac{V_{oc} J_{sc} FF}{P_{in}} \qquad (4)$$

Whereby P_{in} symbolizes the incident light power. Three experimental data (see Table S1 and Fig. S2) of DSSC devices were prepared, and the best data was selected and presented in Table 6. The cost-effectiveness of the prepared samples was estimated using various raw materials used during the synthesis (see supplementary materials Section S2.1). The costs of

the fully prepared DSSC devices were only differentiated using SSFC, RGO-SSFC, and N-RGO-SSFC. The costs of the prepared samples were estimated as R335.43, R5,586.03, R5,836.03, and R16,515.94 for SSFC, RGO-SSFC, N-RGO-SSFC, and Pt, respectively. The use of graphene-based materials in the DSSCs fabrication was considered cost-effective in this study.

The GO counter electrode displays the lowest device performance (PCE = 2.20%), which can be attributed to the lowest J_{sc} (8.79 mA cm^{-2}) caused by poor diffusion characteristics at the electrolyte-electrode interface and poor electron transfer. This indicates that when GO is applied as a counter electrode, it will form an insufficient electrocatalytic activity due to the low electrical conductivity of GO (Table 5), which results in high back electron transfer and low electron injection rate, thus leading to a low V_{oc} (0.61 V). The lower PCE could also be attributed to the insulating nature of GO owing to the absence of percolating pathways at the sp^2-hybridized C-C bonding cluster to facilitate charge carrier transport due to the presence of polar oxygen functional groups with a strong hydrophilic nature. However, RGO improves the device performance (PCE = 3.29%) when compared to GO. The use of RGO as an electrode would contribute to less back electron transfer and improved electron injection rate, due to the removal of oxygenated functional group. However, this lowers the hydrophilic nature of GO, thereby negatively contributing to the deterioration of the electrolyte/electrode interface.

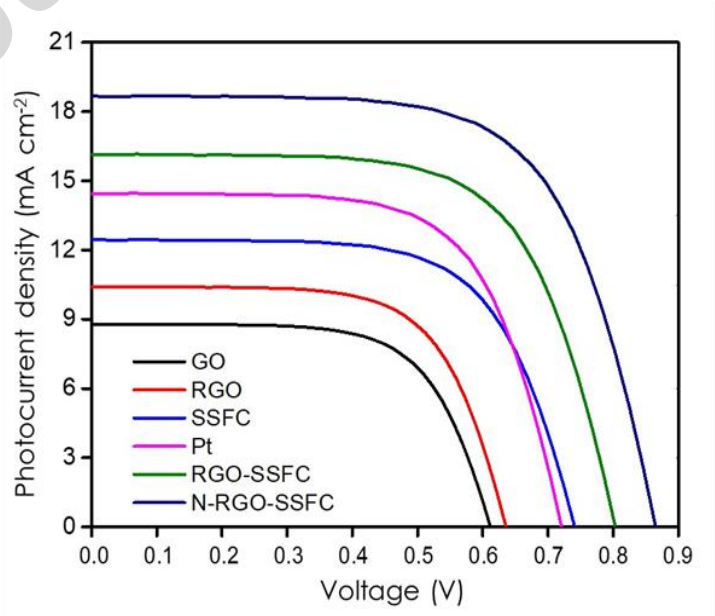

Fig. 13. Photocurrent density-voltage of GO, RGO, SSFC, Pt, RGO-SSFC, and N-RGO-SSFC as electrodes of DSSC devices.

The SSFC counter electrode was observed to have a low V_{oc} (0.73 V) due to the higher aggregation of nanoparticles in SSFC (Fig. 3 (c)) than in RGO-SSFC when used as counter electrodes owing to high charge recombination, which delays dye regeneration. Some aggregated or agglomerated SSFC nanoparticles may affect the electrocatalytic activity on the contact area toward the reduction of I_3^-/I^- electrolyte and result in a low electron injection rate. The DSSCs assembled with SSFC counter electrodes produced a PCE of 4.06%, which was lower than the Pt counter electrode (PCE = 5.52%) as reference. However, the aggregation was reduced upon introducing SSFC nanoparticles to the N-RGO sheets to optimize the surface of SSFC and reduce recombination, thereby increasing the V_{oc}, FF, and PCE.

The introduction of SSFC onto the RGO framework to form RGO-SSFC did alter the basal and edges of GO. It resulted in enhanced electrochemical properties, enriching the RGO-SSFC with high activity. The RGO-SSFC counter electrode reveals the improved device performance (PCE = 5.94%) due to the strong synergistic effect between SSFC and RGO observed in Fig. 5, which enhances a photogenerated charge carriers transportation and collection for redox reaction, resulting in higher J_{sc} (16.04 mA cm^{-2}). The increase in J_{sc} could be attributed to higher optical absorption wavelength (Fig. 8 (b)), resulting in more photogenerated charge carriers. Therefore, RGO-SSFC formation would effectively allow the transportation and collection of electrons from the circuit through the electrochemical site surface due to improved electrical conductivity, as shown in Table 4. On the other side, the created defect active sites during the formation of RGO-SSFC would act as the catalytic sites during the reduction of triiodide, resulting in high energy conversion efficiency on the I_3^-/I^-.

Table 6. Photovoltaic parameters of DSSCs based on various prepared materials counter electrodes.

Cathode samples	V_{oc} (V)	J_{sc} (mA cm^{-2})	FF (%)	PCE (%)	R_{SE} (Ω $cm^{2)}$	R_{SH} (Ω cm^2)
Pt (ref)	0.73	14.50	64	5.52 ± 0.01	8.69	311.67
GO	0.61	8.79	34	2.20 ± 0.02	22.02	38.78

RGO	0.64	10.38	49	3.29 ± 0.02	12.59	70.28
SSFC	0.73	12.44	40	4.06 ± 0.04	10.84	118.10
RGO-SSFC	0.81	16.04	66	5.94 ± 0.01	8.45	389.40
N-RGO-SSFC	0.88	18.63	69	6.64 ± 0.01	3.53	455.56

The doping of N onto RGO-SSFC results in superior device performance (PCE = 6.64%) when used in counter electrode/electrolyte interface, due to high interfacial active sites, high electron mobility, and low R_{ct}. The high V_{oc} of 0.88 V for N-RGO-SSFC was attributed to the decrease in photoinjected electron recombination rate of TiO_2 as the semiconductor with eosin B molecules, which resulted in the improvement in band alignment between the semiconductor TiO_2 interface and the harvester. On the other side, the hydrophobic moieties on the organic dye can improve V_{oc} by shielding photoelectrons in the TiO_2 film to prevent recombination with oxidized iodide liquid electrolyte species [93]. TiO_2 was used to prepare our semiconductor layer. A similar observation was also noted in our previous study [94]. Moreover, using N-RGO-SSFC would enhance the redox kinetic ability of the electrode/electrolyte interface and enrich dye molecule regeneration, as shown in Fig. 11 (e), thus enhancing the J_{sc} and PCE. N-RGO-SSFC was noted to have the highest J_{sc} of 18.63 mA cm^{-2} compared to other prepared materials. The enhancement in J_{sc} can be related to the largest surface area, and electrical conductivity of N-RGO-SSFC observed in Tables 4 and 5, respectively, which positively affect charge transfer at the counter electrode. This indicates the existence of excellent electron transport pathways between the N-RGO sheets and SSFC nanoparticles, which increase the contact area between the counter electrode and the electrolyte. The presence of SSFC nanoparticles on N-RGO sheets produced an efficient catalytic network that maximizes active edge sites during the reduction of triiodide to enhance the efficiency of DSSCs. The FF was reported to have a strong relationship with the counter electrode conductivity, whereby a higher conductivity results in a more considerable FF value. The relatively low FF on the pristine SSFC-based device indicates the existence of high charge carrier recombination (as observed in Fig. 9) and leakage current arising from the aggregation of SSFC nanoparticles, as observed in Fig. 2 (SEM image). However, the FF increased upon forming N-RGO-SSFC, indicating reduced charge carrier recombination and leakage current on the device. Conversely, the good dispersion of SSFC onto N-RGO would be expected to increase the FF.

From the J-V plots in Fig. 13, it can be deduced that the addition of RGO onto SSFC and the doping of N did exhibit a smaller series resistance (R_{SE}) and larger shunt resistance (R_{SH}), Table 6, which contribute to an improvement of FF, when compared to GO, RGO and SSFC cathode samples. The R_{SE} and R_{SH} were calculated as [95]:

$$R_{SE} = {}^{dV}/_{dJ} \quad J = 0 \tag{4}$$

$$R_{SH} = {}^{dV}/_{dJ} \; V = 0 \tag{5}$$

The shunt and series resistances have negligible influence on V_{oc}, while both these resistances influence the J_{sc} value. The introduction of SSFC onto RGO did reveal the smaller $R_{SE,}$ which could be related to the high conductivity (i.e. lower sheet resistance) of RGO-SSFC and N-RGO-SSFC obtained. Conversely, the higher R_{SH} observed on RGO-SSFC and N-RGO-SSFC could be attributed to improved power loss of DSSC devices. In addition, the decrease in R_{SE} and increase of R_{SH} of RGO-SSFC and N-RGO-SSFC were attributed to the enhanced FF, thus resulting in higher efficiencies.

N-RGOS-SSFC reveals an enhanced device performance due to relatively excellent electrocatalytic activity that would positively contribute to reducing iodine electrolytes. The high PCE of the N-RGO-SSFC-based device could be due to the presence of metal ions on perovskites with mixed valences, which can afford the electron hopping between Fe^{3+} and Co^{3+} to Fe^{4+} and Co^{4+}, allowing the N-RGO-SSFC to be the ideal catalyst to reduce electrolyte and effective collect electrons from the external circuit [96]. A similar observation was noted by Yang et al. [69] when doping $La_{0.7}Ca_{0.3}MnO_3$ onto N-RGO to form a bifunctional catalyst. Also, the high surface area of N-RGO-SSFC can lead to an increase in the active sites due to the strong chemical coupling between SSFC and N-RGO, which prevents the agglomeration of SSFC on the N-RGO sheets. This results in larger contact with the electrolyte and more active sites for the triiodide reduction. The strong interaction between mixed valent perovskite oxide SSFC and N-RGO sheets can enhance the performance of the device. On the other side, N would stimulate the electrocatalytic activity of RGO-SSFC. Using N-RGO-SSFC as a counter electrode is less expensive when compared to platinum, allowing N-RGO-SSFC to be a potential counter-electrode candidate for replacing platinum in DSSCs.

4. Conclusion

In summary, the effect of using SSFC, GO, RGO, RGO-SSFC, and N-RGO-SSFC counter electrodes on DSSC performance was demonstrated. The XRD, FTIR, Raman, and XRD analysis confirmed the SSFC, GO, RGO, RGO-SSFC, and N-RGO-SSFC structural formation. A body-centred tetragonal structure of SSFC was successfully introduced to RGO while doping with N. The SEM and elemental analysis revealed the SSFC nanoparticles were uniformly distributed on the RGO and N-RGO sheets. IR revealed a decrease in oxygenated functional groups from GO to RGO. The remaining oxygen functional groups were used to anchor the SSFC nanoparticles to form more defects and active sites on the RGO and N-RGO sheets, which assisted in reducing the electrolyte. The strong interaction between SSFC nanoparticles and N-RGO sheets improved the electrochemical properties as a result of a larger surface area and enhanced electrical conductivity. The DSSCs equipped with N-RGO-SSFC as a counter electrode exhibited the best PCE of 6.64%, which exceeded 5.52% for the Pt-based reference devices, demonstrating the suitability of N-RGO-SSFC as a potential candidate for counter electrode fabrication in DSSCs.

Author contributions

Conceptualisation, S.N., E.M., M.A.O. and V.O.N.; methodology, S.N., E.M., M.A.O. and V.O.N.; software, S.N., E.M., M.O.A. and V.O.N.; validation, S.N., E.M., M.O.A. and V.O.N.; formal analysis, S.N., E.M., M.O.A. and V.O.N.; investigation, S.N., E.M., M.O.A. and V.O.N.; resources, V.O.N.; data curation, S.N., E.M., M.O.A. and V.O.N.; writing-original draft preparation, S.N., E.M., M.O.A. and V.O.N.; writing-review and editing, S.N.; visualisation, S.N., E.M., M.O.A. and V.O.N.; supervision, V.O.N.; project administration, V.O.N.; funding acquisition, V.O.N.

Conflict of interest

The authors declare that they have no conflict of interest.

Acknowledgements

The authors express gratitude to the University of KwaZulu-Natal (UKZN); National Research Foundation (NRF) under Grant numbers 107740, 145770, 103979, and 121165; Moses Kotane Institution, UKZN Nanotechnology Platform and Eskom Tertiary Education Support Programme (TESP) for their support and funding of this research.

References

[1] S. Yoon, E.-Y. Shin, N.-K. Cho, S. Park, H. Y. Woo, H. J. Son, Progress in morphology control from fullerene to nonfullerene acceptors for scalable high-performance organic photovoltaics, J. Mater. Chem. A. 9 (2021) 24729. https://doi.org/10.1039/D1TA06861J.

[2] M. Kokkonen, P. Talebi, J. Zhou, S. Asgari, S. A. Soomro, F. Elsehrawy, J. Halme, S. Ahmad, A. Hagfeldt, S. G. Hashmi, Advanced research trends in dye-sensitized solar cells, J. Mater. Chem. A. 9 (2021) 10527. https://doi.org/10.1039/D1TA00690H.

[3] A. M. Mahran, S. O. Abdellatif, Transparency against efficiency in uni/bifacial mesostructured-based solar cells for self-powered sensing applications, Analog Integr. Circuits and Signal Processing. 114 (2023) 217. https://doi.org/10.1007/s10470-022-02114-y.

[4] S. O. Abdellatif, S. Josten, A. S. Khalil, D. Erni, F. Marlow, Transparency and diffused light efficiency of dye-sensitized solar cells: tuning and a new figure of merit, IEEE J. Photovolt. 10 (2020) 522. https://doi.org/10.1109/JPHOTOV.2020.2965399.

[5] D. Devadiga, M. Selvakumar, P. Shetty, M. S. Santosh, The integration of flexible dye-sensitized solar cells and storage devices towards wearable self-charging power systems: a review, Renew. Sust. Energ. Rev. 159 (2022) 112252. https://doi.org/10.1016/j.rser.2022.112252.

[6] X. Wang, S. Karanjit, L. Zhang, H. Fong, Q. Qiao, Z. Zhu, Transient photocurrent and photovoltage studies on charge transport in dye sensitized solar cells made from the composites of TiO_2 nanofibers and nanoparticles, Appl. Phy. Lett. 98 (2011) 082114. https://doi.org/10.1063/1.3560057.

[7] J. M. Cole, K. S. Low, H. Ozoe, P. Stathi, C. Kitamura, H. Kurata, P. Rudolf, T. Kawase, Data mining with molecular design rules identifies new class of dyes for dye-sensitised solar cells, Phys. Chem. Chem. Phys. 16 (2014) 26684. https://doi.org/10.1039/C4CP02645D.

[8] E. Nosheen, S. M. Shah, H. Hussain, G. Murtaza, Photo-sensitization of ZnS nanoparticles with renowned ruthenium dyes N3, N719 and Z907 for application in solid state dye sensitized solar cells: a comparative study, J. Photochem. Photobiol. B, Biol. 162 (2016) 583. https://doi.org/10.1016/j.jphotobiol.2016.07.033.

[9] A. S. Najm, S. A. Alwash, N. H. Sulaiman, M. Chowdhury, K. Techato, N719 dye as a sensitizer for dye-sensitized solar cells (DSSCs): a review of its functions and certain

rudimentary principles, Environ. Prog. Sustain. Energy. 42 (2023) e13955. https://doi.org/10.1002/ep.13955.

[10] Q. Yu, Y. Wang, Z. Yi, N. Zu, J. Zhang, M. Zhang, P. Wang, High-efficiency dye-sensitized solar cells: the influence of lithium ions on exciton dissociation, charge recombination, and surface states, ACS Nano. 4 (2010) 6032. https://doi.org/10.1021/nn101384e.

[11] L. Jin, S. Shi, C. Zhao, X. Yu, J. Lu, Q. Wang, Y. Wei, Y-shaped organic dyes with D_2–π–A configuration as efficient co-sensitizers for ruthenium-based dye sensitized solar cells, J. Power Sources. 481 (2021) 228952. https://doi.org/10.1016/j.jpowsour.2020.228952.

[12] S. H. Kang, M. J. Jeong, Y. K. Eom, I. T. Choi, S. M. Kwon, Y. Yoo, J. Kim, J. Kwon, J. H. Park, H. K. Kim, Porphyrin sensitizers with donor structural engineering for superior performance dye-sensitized solar cells and tandem solar cells for water splitting applications, Adv. Energy Mater. 7 (2017) 1602117. https://doi.org/10.1002/aenm.201602117.

[13] J.-M. Ji, H. Zhou, H. K. Kim, Rational design criteria for D–π–A structured organic and porphyrin sensitizers for highly efficient dye-sensitized solar cells, J. Mater. Chem. A. 6 (2018) 14518. https://doi.org/10.1039/C8TA02281J.

[14] H. Zhou, H. J. Lee, Masud, M. Aftabuzzaman, S. H. Kang, C. H. Kim, H. M. Kim, H. K. Kim, Synergistic effect of size-tailored structural engineering and postinterface modification for highly efficient and stable dye-sensitized solar cells, ACS Appl. Mater. Interfaces. 15 (2023) 43835. https://doi.org/10.1021/acsami.3c09228.

[15] Y. Ren, D. Zhang, J. Suo, Y. Cao, F. T. Eickemeyer, N. Vlachopoulos, S. M. Zakeeruddin, A. Hagfeldt, M. Grätzel, Hydroxamic acid pre-adsorption raises the efficiency of cosensitized solar cells, Nature. 613 (2023) 60. https://doi.org/10.1038/s41586-022-05460-z.

[16] J. M. Ji, H. Zhou, Y. K. Eom, C. H. Kim, H. K. Kim, 14.2% efficiency dye-sensitized solar cells by co-sensitizing novel thieno [3,2-b] indole-based organic dyes with a promising porphyrin sensitizer, Adv. Energy Mater. 10 (2020) 2000124. https://doi.org/10.1002/aenm.202000124.

[17] A. Yella, H.-W. Lee, H. N. Tsao, C. Yi, A. K. Chandiran, M. K. Nazeeruddin, E. W.-G. Diau, C.-Y. Yeh, S. M. Zakeeruddin, M. Grätzel, Porphyrin-sensitized solar cells with cobalt (II/III)–based redox electrolyte exceed 12 percent efficiency, Science. 334 (2011) 629. https://doi.org/10.1126/science.1209688.

[18] M. Ye, X. Wen, M. Wang, J. Iocozzia, N. Zhang, C. Lin, Z. Lin, Recent advances in dye-sensitized solar cells: from photoanodes, sensitizers and electrolytes to counter electrodes, Mater. Today. 18 (2015) 155. https://doi.org/10.1016/j.mattod.2014.09.001.

[19] H. Zhou, H. K. Kim, Effective redox shuttles for polymer gel electrolytes-based quasi-solid-state dye-sensitized solar cells in outdoor and indoor applications: comprehensive comparison and guidelines, Mater. Today Energy. 34 (2023) 101299. https://doi.org/10.1016/j.mtener.2023.101299.

[20] J. D. Roy-Mayhew, I. A. Aksay, Graphene materials and their use in dye-sensitized solar cells, Chem. Rev. 114 (2014) 6323. https://doi.org/10.1021/cr400412a.

[21] C.-K. Cheng, C.-H. Lin, H.-C. Wu, C.-C. M. Ma, T.-K. Yeh, H.-Y. Chou, C.-H. Tsai, C.-K. Hsieh, The two-dimensional nanocomposite of molybdenum disulfide and nitrogen-doped graphene oxide for efficient counter electrode of dye-sensitized solar cells, Nanoscale Res. Lett. 11 (2016) 1. https://doi.org/10.1186/s11671-016-1277-0.

[22] K. Zhang, M. W. Khan, X. Zuo, Q. Yang, H. Tang, M. Wu, G. Li, Controllable synthesis and photoelectric properties of interconnected and self-assembled nanocomposite of porous hollow Cu_7S_4/CuS and nitrogen-doped graphene oxide, Electrochim. Acta. 307 (2019) 64. https://doi.org/10.1016/j.electacta.2019.03.173.

[23] I. Ahmad, U. Khan, Y. K. Gun'ko, Graphene, carbon nanotube and ionic liquid mixtures: towards new quasi-solid state electrolytes for dye sensitised solar cells, J. Mater. Chem. 21 (2011) 16990. https://doi.org/10.1039/C1JM11537E.

[24] K. Xiong, G. Li, C. Jin, S. Jin, $La_{0.65}Sr_{0.35}MnO_3$@RGO nanocomposites as an effective counter electrode for dye-sensitized solar cells, Mater Lett. 164 (2016) 609. https://doi.org/10.1016/j.matlet.2015.10.143.

[25] I.-Y. Jeon, H. M. Kim, I. T. Choi, K. Lim, J. Ko, J. C. Kim, H.-J. Choi, M. J. Ju, J.-J. Lee, H. K. Kim, High-performance dye-sensitized solar cells using edge-halogenated graphene nanoplatelets as counter electrodes, Nano Energy. 13 (2015) 336. https://doi.org/10.1016/j.nanoen.2015.02.037.

[26] D. Zhang, X. Li, H. Li, S. Chen, Z. Sun, X. Yin, S. Huang, Graphene-based counter electrode for dye-sensitized solar cells, Carbon. 49 (2011) 5382. https://doi.org/10.1016/j.carbon.2011.08.005.

[27] C. K. Kim, J.-M. Ji, M. Aftabuzzaman, H. K. Kim, Three-dimensional tellurium and nitrogen Co-doped mesoporous carbons for high performance supercapacitors, RSC Adv. 11 (2021) 8628. https://doi.org/10.1039/D0RA10374H.

[28] M. Aftabuzzaman, C. Lu, H. K. Kim, Recent progress on nanostructured carbon-based counter/back electrodes for high-performance dye-sensitized and perovskite solar cells, Nanoscale. 12 (2020) 17590. https://doi.org/10.1039/D0NR04112B.

[29] C. K. Kim, J.-M. Ji, H. Zhou, C. Lu, H. K. Kim, Tellurium-doped, mesoporous carbon nanomaterials as transparent metal-free counter electrodes for high-performance bifacial dye-sensitized solar cells, Nanomaterials. 10 (2019) 29. https://doi.org/10.3390/nano10010029.

[30] M. Aftabuzzaman, C. K. Kim, H. Zhou, H. K. Kim, In situ preparation of Ru–N-doped template-free mesoporous carbons as a transparent counter electrode for bifacial dye-sensitized solar cells, Nanoscale. 12 (2020) 1602. https://doi.org/10.1039/C9NR09019C.

[31] M. Aftabuzzaman, C. K. Kim, T. Kowalewski, K. Matyjaszewski, H. K. Kim, A facile route to well-dispersed Ru nanoparticles embedded in self-templated mesoporous carbons for high-performance supercapacitors, J.Mater. Chem. A. 7 (2019) 20208. https://doi.org/10.1039/C9TA06571G.

[32] S. Hwang, J. Moon, S. Lee, D.-H. Kim, D. Lee, W. Choi, M. Jeo, Carbon nanotubes as counter electrode for dye-sensitised solar cells, Electron. Lett. 43 (2007) 1455. https://doi.org/10.1049/el:20072867

[33] C.-S. Wu, T.-W. Chang, H. Teng, Y.-L. Lee, High performance carbon black counter electrodes for dye-sensitized solar cells, Energy. 115 (2016) 513. https://doi.org/10.1016/j.energy.2016.09.052.

[34] J.-M. Ji, C. K. Kim, H. K. Kim, Well-dispersed Te-doped mesoporous carbons as Pt-free counter electrodes for high-performance dye-sensitized solar cells, Dalton Trans. 50 (2021) 9399. https://doi.org/10.1039/D0DT04372A.

[35] M. J. Ju, I. T. Choi, M. Zhong, K. Lim, J. Ko, J. Mohin, M. Lamson, T. Kowalewski, K. Matyjaszewski, H. K. Kim, Copolymer-templated nitrogen-enriched nanocarbons as a low charge-transfer resistance and highly stable alternative to platinum cathodes in dye-sensitized solar cells, J. Mater. Chem. A. 3 (2015) 4413. https://doi.org/10.1039/C4TA07012G.

[36] S. Visnupriya, N. Prabavathi, P. Vijayakumar, N. Santhosh, K. Pradeeswari, Bimetallic-reduced graphene oxide nanocomposites as a reactive counter electrodes for dye sensitized solar cells, J. Mater. Sci. Mater. Electronics. (2022) 1. https://doi.org/10.1007/s10854-022-07748-2.

[37] Y. Zhang, Z. Gao, N. Song, J. He, X. Li, Graphene and its derivatives in lithium–sulfur batteries, Mater. Today Energy. 9 (2018) 319. https://doi.org/10.1016/j.mtener.2018.06.001.

[38] C. K. Kim, H. M. Kim, M. Aftabuzzaman, I.-Y. Jeon, S. H. Kang, Y. K. Eom, J. B. Baek, H. K. Kim, Comparative study of edge-functionalized graphene nanoplatelets as metal-free counter electrodes for highly efficient dye-sensitized solar cells, Mater. Today Energy. 9 (2018) 67. https://doi.org/10.1016/j.mtener.2018.05.003.

[39] M. H. Yeh, L. Y. Lin, L. Y. Chang, Y. A. Leu, W. Y. Cheng, J. J. Lin, K. C. Ho, Dye-sensitized solar cells with reduced graphene oxide as the counter electrode prepared by a green photothermal reduction process, ChemPhysChem. 15 (2014) 1175. https://doi.org/10.1002/cphc.201301128.

[40] A. Karaphun, C. Phrompet, W. Tuichai, N. Chanlek, C. Sriwong, C. Ruttanapun, The influence of annealing on a large specific surface area and enhancing electrochemical properties of reduced graphene oxide to improve the performance of the active electrode of supercapacitor devices, Mater. Sci. Eng B. 264 (2021) 114941. https://doi.org/10.1016/j.mseb.2020.114941.

[41] J.-Y. Tak, S. H. Jin, W. H. Nam, J. Y. Cho, W.-S. Seo, G.-G. Lee, H. K. Cho, Y. S. Lim, Significantly enhanced chemical stability in interface-controlled $Cu_{2+x}Se$-reduced graphene oxide composites and related thermoelectric performances, J. Eur. Ceram. Soc. 41 (2021) 459. https://doi.org/10.1016/j.jeurceramsoc.2020.08.023.

[42] B. Guo, X. Ji, W. Wang, X. Chen, P. Wang, L. Wang, J. Bai, Highly flexible, thermally stable, and static dissipative nanocomposite with reduced functionalized graphene oxide processed through 3D printing, Compos. B Eng. 208 (2021) 108598. https://doi.org/10.1016/j.compositesb.2020.108598.

[43] R. A. Lima, A. J. Pinto, L. A. Pocrifka, R. R. Passos, Investigation of nitrogen-doping influence on the electrocatalytic activity of graphene in alkaline oxygen reduction reaction, Mater. Res. 24 (2021) 1. https://doi.org/10.1590/1980-5373-MR-2020-0375.

[44] Z. Chu, Y. Wang, L. Jiao, X. Zhang, Laser-scribed reduced graphene oxide as counter electrode for dye-sensitized solar cell, Fuller. Nanotub. Carbon Nanostructures. 27 (2019) 914. https://doi.org/10.1080/1536383X.2019.1660648.

[45] V. Loryuenyong, S. Yaotrakool, P. Prathumted, J. Lertsiri, A. Buasri, Synergistic effects of graphene–polyaniline counter electrode in dye-sensitised solar cells, Micro Nano Lett. 11 (2016) 77. https://doi.org/10.1049/mnl.2015.0363.

[46] W. Yang, X. Xu, Z. Tu, Z. Li, B. You, Y. Li, S. I. Raj, F. Yang, L. Zhang, S. Chen, Nitrogen plasma modified CVD grown graphene as counter electrodes for bifacial dye-sensitized solar cells, Electrochim. Acta. 173 (2015) 715. https://doi.org/10.1016/j.electacta.2015.05.143.

[47] L. J. Brennan, M. T. Byrne, M. Bari, Y. K. Gun'ko, Carbon nanomaterials for dye-sensitized solar cell applications: a bright future, Adv. Energy Mater. 1 (2011) 472. https://doi.org/10.1002/aenm.201100136.

[48] H. Liu, Y. Liu, D. Zhu, Chemical doping of graphene, J. Mater. Chem. 21 (2011) 3335. https://doi.org/10.1039/C0JM02922J.

[49] M. J. Ju, J. C. Kim, H.-J. Choi, I. T. Choi, S. G. Kim, K. Lim, J. Ko, J.-J. Lee, I.-Y. Jeon, J.-B. Baek, N-doped graphene nanoplatelets as superior metal-free counter electrodes for organic dye-sensitized solar cells, ACS Nano. 7 (2013) 5243. https://doi.org/10.1021/nn4009774.

[50] P. A. Denis, Heteroatom codoped graphene: the importance of nitrogen, ACS omega. 7 (2022) 45935. https://doi.org/10.1021/acsomega.2c06010.

[51] Z. He, W. Que, Y. Xing, X. Liu, Reporting performance in MoS_2–TiO_2 bilayer and heterojunction films based dye-sensitized photovoltaic devices, J. Alloys Compd. 672 (2016) 481. https://doi.org/10.1016/j.jallcom.2016.02.186.

[52] D. Long, W. Li, L. Ling, J. Miyawaki, I. Mochida, S.-H. Yoon, Preparation of nitrogen-doped graphene sheets by a combined chemical and hydrothermal reduction of graphene oxide, Langmuir. 26 (2010) 16096. https://doi.org/10.1021/la102425a.

[53] C. Rao, K. Gopalakrishnan, A. Govindaraj, Synthesis, properties and applications of graphene doped with boron, nitrogen and other elements, Nano Today. 9 (2014) 324. https://doi.org/10.1016/j.nantod.2014.04.010.

[54] M. Yu, J. Zhang, S. Li, Y. Meng, J. Liu, Three-dimensional nitrogen doped holey reduced graphene oxide framework as metal-free counter electrodes for high performance dye-sensitized solar cells, J. Power Sources. 308 (2016) 44. https://doi.org/10.1016/j.jpowsour.2016.01.025.

[55] J. Ma, W. Shen, F. Yu, Graphene-enhanced three-dimensional structures of MoS_2 nanosheets as a counter electrode for Pt-free efficient dye-sensitized solar cells, J Power Sources. 351 (2017) 58. https://doi.org/10.1016/j.jpowsour.2017.03.047.

[56] M. Z. Iqbal, S. Khan, Progress in the performance of dye sensitized solar cells by incorporating cost effective counter electrodes, Sol. Energy. 160 (2018) 130. https://doi.org/10.1016/j.solener.2017.11.060.

[57] A. Alizadeh, Z. Shariatinia, Unveiling the influence of $SmFeO_3$-TiO_2 nanocomposites as high performance photoanodes of dye-sensitized solar cells, J. Mol Liq. 348 (2022) 118070. https://doi.org/10.1016/j.molliq.2021.118070.

[58] J. Seok, A. s. Molina Villarino, Z. Shi, Y. Yang, M. Ahmadi, D. A. Muller, F. J. DiSalvo, H. D. Abruña, La-based perovskite oxide catalysts for alkaline oxygen reduction: the importance of electrochemical stability, J. Phys. Chem. C. 126 (2022) 3098. https://doi.org/10.1021/acs.jpcc.2c00108.

[59] Q. Yang, J. Yao, K. Zhang, W. Wang, X. Zuo, H. Tang, M. Wu, G. Li, Perovskite-type $La_{1-x}Ca_xMnO_3$ manganese oxides as effective counter electrodes for dye-sensitized solar cells, J. Electroanal. Chem. 833 (2019) 1. https://doi.org/10.1016/j.jelechem.2018.11.006.

[60] Y.-R. Sun, X. Zhang, L.-G. Wang, Z.-K. Liu, N. Kang, N. Zhou, W.-L. You, J. Li, X.-F. Yu, Lattice contraction tailoring in perovskite oxides towards improvement of oxygen electrode catalytic activity, Chem. Eng. J. 421 (2021) 129698. https://doi.org/10.1016/j.cej.2021.129698.

[61] X. Guo, X. Kong, D. Wu, Y. Sun, L. Li, L. Sun, J. Zhang, Evaluation of three-dimensionally ordered macroporous $LaFe_{1-x}Co_xO_3$ perovskites and their performance for catalytic oxidation of methane, Mater. Today Commun. 32 (2022) 103905. https://doi.org/10.1016/j.mtcomm.2022.103905.

[62] T. V. Raj, P. A. Hoskeri, H. Muralidhara, C. Manjunatha, K. Y. Kumar, M. Raghu, Facile synthesis of perovskite lanthanum aluminate and its green reduced graphene oxide composite for high performance supercapacitors, J. Electroanal. Chem. 852 (2020) 113830. https://doi.org/10.1016/j.jelechem.2020.113830.

[63] T. Lv, Z. Xu, W. Hong, G. Li, Y. Li, L. Jia, Graphene oxide mediated self-sacrificial synthesis of $LaCO_3OH$-$Ni(OH)_2$@graphene hierarchical composite for photocatalytic H2 evolution and supercapacitor, Chem. Eng. J. 382 (2020) 123021. https://doi.org/10.1016/j.cej.2019.123021.

[64] S. R. Choi, I.-S. So, S. W. Lee, J. Yoo, Y.-S. Seo, H.-S. Cho, J.-Y. Park, 3D architecture double perovskite $NdBa_{0.5}Sr_{0.5}Co_{1.5}Fe_{0.5}O_{5+\delta}$ embedded hollow-net Co_3O_4 bifunctional electrocatalysts coupled with N-doped CNT and reduced graphene oxide for oxygen electrode reactions, J. Alloys Compd. (2020) 153782. https://doi.org/10.1016/j.jallcom.2020.153782.

[65] E. El-Khawas, A. Azab, A. Mansour, Structural, magnetic and dielectric properties of reduced graphene oxide/$La_{0.9}Bi_{0.1}FeO_3$ nanocomposites, Mater. Chem. Phy. 241 (2020) 122335. https://doi.org/10.1016/j.matchemphys.2019.122335.

[66] K. Xiong, G. Li, C. Jin, S. Jin, $La_{0.65}Sr_{0.35}MnO_3$@RGO nanocomposites as an effective counter electrode for dye-sensitized solar cells, Mater. Lett. 164 (2016) 609. https://doi.org/10.1016/j.matlet.2015.10.143.

[67] F. Noori, A. Gholizadeh, Structural, optical, magnetic properties and visible light photocatalytic activity of $BiFeO_3$/graphene oxide nanocomposites, Mater. Res. Express. 6 (2020) 1250. https://doi.org/10.1088/2053-1591/ab6807.

[68] K. Xiong, G. Li, C. Jin, S. Jin, $La_{0.65}Sr_{0.35}MnO_3$@RGO nanocomposites as an effective counter electrode for dye-sensitized solar cells, Mater. Lett. 164 (2016) 609. https://doi.org/10.1016/j.matlet.2015.10.143.

[69] Q. Yang, X. Zuo, J. Yao, K. Zhang, H. Zhang, M. W. Khan, W. Wang, H. Tang, M. Wu, G. Li, $La_{0.7}Ca_{0.3}MnO_3$ nanoparticles anchored on N-doped graphene: highly efficient bifunctional catalyst as counter electrode for dye-sensitized solar cells, J. Electroanal. Chem. 844 (2019) 34. https://doi.org/10.1016/j.jelechem.2019.05.014.

[70] W. S. Hummers Jr, R. E. Offeman, Preparation of graphitic oxide, J. Am. Chem. Soc. 80 (1958) 1339. https://doi.org/10.1021/ja01539a017.

[71] C. Botas, P. Álvarez, P. Blanco, M. Granda, C. Blanco, R. Santamaría, L. J. Romasanta, R. Verdejo, M. A. López-Manchado, R. Menéndez, Graphene materials with different structures prepared from the same graphite by the Hummers and Brodie methods, Carbon. 65 (2013) 156. https://doi.org/10.1016/j.carbon.2013.08.009.

[72] S. Carbonin, F. Martignago, G. Menegazzo, A. Dal Negro, X-ray single-crystal study of spinels: in situ heating, Phys. Chem. Miner. 29 (2002) 503. https://doi.org/10.1007/s00269-002-0262-6.

[73] L. Kumar, P. Kumar, A. Narayan, M. Kar, Rietveld analysis of XRD patterns of different sizes of nanocrystalline cobalt ferrite, Int. Nano Lett. 3 (2013) 1. https://doi.org/10.1186/2228-5326-3-8.

[74] M. N. Sithole, B. Omondi, P. G. Ndungu, Synthesis and characterization of $Ce_{0.6}Sr_{0.4}Fe_{0.8}Co_{0.2}O_{3-\delta}$ perovskite material: Potential cathode material for low temperature SOFCs, J. Rare Earths. 35 (2017) 389. https://doi.org/10.1016/S1002-0721(17)60924-4.

[75] K. Yokwana, S. C. Ray, M. Khenfouch, A. T. Kuvarega, B. B. Mamba, S. D. Mhlanga, E. N. Nxumalo, Facile synthesis of nitrogen doped graphene oxide from graphite

flakes and powders: a comparison of their surface chemistry, J. Nanosci. Nanotechnol. 18 (2018) 5470. https://doi.org/10.1166/jnn.2018.15429.

[76] R. Riaz, M. Ali, I. A. Sahito, A. A. Arbab, T. Maiyalagan, A. S. Anjum, M. J. Ko, S. H. Jeong, Self-assembled nitrogen-doped graphene quantum dots (N-GQDs) over graphene sheets for superb electro-photocatalytic activity, Appl. Surf. Sci. 480 (2019) 1035. https://doi.org/10.1016/j.apsusc.2019.02.228.

[77] E. Singh, H. S. Nalwa, Graphene-based dye-sensitized solar cells: a review, Sci. Adv. Mater. 7 (2015) 1863. https://doi.org/10.1166/sam.2015.2438.

[78] L. Wei, P. Wang, Y. Yang, R. Luo, J. Li, X. Gu, Z. Zhan, Y. Dong, W. Song, R. Fan, Facile synthesis of nitrogen-doped reduced graphene oxide as an efficient counter electrode for dye-sensitized solar cells, J. Nanopart. Res. 20 (2018) 1. https://doi.org/10.1007/s11051-018-4203-9.

[79] J. W. Lee, A. S. Hall, J.-D. Kim, T. E. Mallouk, A facile and template-free hydrothermal synthesis of Mn_3O_4 nanorods on graphene sheets for supercapacitor electrodes with long cycle stability, Chem. Mater. 24 (2012) 1158. https://doi.org/10.1021/cm203697w.

[80] H. Kim, S.-W. Kim, J. Hong, Y.-U. Park, K. Kang, Electrochemical and ex-situ analysis on manganese oxide/graphene hybrid anode for lithium rechargeable batteries, J. Mater Res. 26 (2011) 2665. https://doi.org/10.1557/jmr.2011.301.

[81] Y. Qiu, F. Guo, R. Hurt, I. Külaots, Explosive thermal reduction of graphene oxide-based materials: mechanism and safety implications, Carbon. 72 (2014) 215. https://doi.org/10.1016/j.carbon.2014.02.005.

[82] N. Chakrabarty, A. Dey, S. Krishnamurthy, A. K. Chakraborty, CeO_2/Ce_2O_3 quantum dot decorated reduced graphene oxide nanohybrid as electrode for supercapacitor, Appl. Surf. Sci. 536 (2021) 147960. https://doi.org/10.1016/j.apsusc.2020.147960.

[83] S. Liu, Y. Wang, Z. Ma, Bi_2O_3 with reduced graphene oxide composite as a supercapacitor electrode, Int. J. Electrochem. Sci. 13 (2018) 12256. https://doi.org/10.20964/2018.12.10.

[84] D. R. Cooper, B. D'Anjou, N. Ghattamaneni, B. Harack, M. Hilke, A. Horth, N. Majlis, M. Massicotte, L. Vandsburger, E. Whiteway, Experimental review of graphene, Int. Sch. Res. Notices. 2012 (2012) 1. http://doi.org/10.5402/2012/501686.

[85] N. P. Ngidi, E. Muchuweni, V. O. Nyamori, Dual heteroatom-doped reduced graphene oxide and its application in dye-sensitized solar cells, Opt. Mater. 122 (2021) 111689. https://doi.org/10.1016/j.optmat.2021.111689.

[86] G. Xie, K. Zhang, B. Guo, Q. Liu, L. Fang, J. R. Gong, Graphene-based materials for hydrogen generation from light-driven water splitting, Adv. Mater. 25 (2013) 3820. https://doi.org/10.1002/adma.201301207.

[87] A. Hagfeldt, G. Boschloo, L. Sun, L. Kloo, H. Pettersson, Dye-sensitized solar cells, Chem. Rev. 110 (2010) 6595. https://doi.org/10.1021/cr900356p.

[88] E. Meyer, R. Taziwa, D. Mutukwa, N. Zingwe, A review on the advancement of ternary alloy counter electrodes for use in dye-sensitised solar cells, Metals. 8 (2018) 1080. https://doi.org/10.3390/met8121080.

[89] D. Chen, H. Feng, J. Li, Graphene oxide: preparation, functionalization, and electrochemical applications, Chem. Rev. 112 (2012) 6027. https://doi.org/10.1021/cr300115g.

[90] S. Nayak, A. Soam, J. Nanda, C. Mahender, M. Singh, D. Mohapatra, R. Kumar, Sol–gel synthesized $BiFeO_3$–graphene nanocomposite as efficient electrode for supercapacitor application, J. Mater. Sci. Mater. Electronic. 29 (2018) 9361. https://doi.org/10.1007/s10854-018-8967-6.

[91] S. Ci, Z. Wen, Y. Qian, S. Mao, S. Cui, J. Chen, NiO-microflower formed by nanowire-weaving nanosheets with interconnected Ni-network decoration as supercapacitor electrode, Sci. Rep. 5 (2015) 1. https://doi.org/10.1038/srep11919.

[92] A. Yadav, A. Lokhande, R. Pujari, J. Kim, C. Lokhande, The synthesis of multifunctional porous honey comb-like La_2O_3 thin film for supercapacitor and gas sensor applications, J. Colloid Interface Sci. 484 (2016) 51. https://doi.org/10.1016/j.jcis.2016.08.056.

[93] S.-R. Jang, K. Zhu, M. J. Ko, K. Kim, C. Kim, N.-G. Park, A. J. Frank, Voltage-enhancement mechanisms of an organic dye in high open-circuit voltage solid-state dye-sensitized solar cells, ACS Nano. 5 (2011) 8267. https://doi.org/10.1021/nn2029567.

[94] S. Ndlovu, E. Muchuweni, M. A. Ollengo, V. O. Nyamori, Tuning the properties of reduced graphene oxide-$Sr_{0.7}Sm_{0.3}Fe_{0.4}Co_{0.6}O_3$ nanocomposites as potential photoanodes for dye-sensitized solar cells, J. Electron. Mater. 52 (2023) 5843. https://doi.org/10.1007/s11664-023-10526-3.

[95] C. Jiang, X. Sun, K. Tan, G. Lo, A. Kyaw, D. Kwong, High-bendability flexible dye-sensitized solar cell with a nanoparticle-modified ZnO-nanowire electrode, Appl. Phys. Lett. 92 (2008) 1. https://doi.org/10.1063/1.2905271.

[96] M. Prabu, P. Ramakrishnan, S. Shanmugam, $CoMn_2O_4$ nanoparticles anchored on nitrogen-doped graphene nanosheets as bifunctional electrocatalyst for rechargeable zinc–air battery, Electrochem. Commun. 41 (2014) 59. https://doi.org/10.1016/j.elecom.2014.01.027.

Author contributions

Conceptualization, S.N., E.M. and V.O.N.; methodology, S.N., E.M. and V.O.N.; software, S.N., E.M. and V.O.N.; validation, S.N., E.M. and V.O.N.; formal analysis, S.N., E.M. and V.O.N.; investigation, S.N., E.M. and V.O.N.; resources, V.O.N.; data curation, S.N., E.M. and V.O.N.; writing—original draft preparation, S.N., E.M. and V.O.N.; writing—review and editing, S.N.; visualization, S.N., E.M. and V.O.N.; supervision, V.O.N.; project administration, V.O.N.; funding acquisition, V.O.N.

Declaration of interests

☒ The authors declare that they have no known competing financial interests or personal relationships that could have appeared to influence the work reported in this paper.

☐ The authors declare the following financial interests/personal relationships which may be considered as potential competing interests:

Highlights

- SSFC did form a tetragonal structure with I4/mmm space group.
- SSFC nanoparticles with the crystallite size of 21.0 nm fully decorated N-RGO sheets.
- N-RGO-SSFC formation revealed increased surface area, high electrical conductivity, and enhanced optical and electrochemical properties.
- N-RGO-SSFC, as the counter electrode, exhibited a PCE of 6.64%, which outperformed the Pt PCE of 5.52%.